Thermal Resistance Measurements of Triply Periodic Minimal Surface Structures (TPMS) of the Thermogalvanic Brick

by

Emmanuel Dasinor

A Thesis Presented in Partial Fulfillment
of the Requirement for the Degree
Master of Science

Approved April 2020 by the
Graduate Supervisory Committee:

Patrick Phelan, Chair
Ryan Milcarek
Dhruv Bhate

ARIZONA STATE UNIVERSITY

May 2020

ABSTRACT

The presence of huge amounts of waste heat and the constant demand for electric energy makes this an appreciable research topic, yet at present there is no commercially viable technology to harness the inherent energy resource provided by the temperature differential between the inside and outside of buildings. In a newly developed technology, electricity is generated from the temperature gradient between building walls through a Seebeck effect. A 3D-printed triply periodic minimal surface (TPMS) structure is sandwiched in copper electrodes with copper (I) sulphate (Cu_2SO_4) electrolyte to mimic a thermogalvanic cell. Previous studies mainly concentrated on mechanical properties and the electric power generation ability of these structures; however, the goal of this study is to estimate the thermal resistance of the 3D-printed TPMS experimentally. This investigation elucidates their thermal resistances which in turn helps to appreciate the power output associated in the thermogalvanic structure. Schwarz P, Gyroid, IWP, and Split P geometries were considered for the experiment with electrolyte in the thermogalvanic brick. Among these TPMS structures, Split P was found more thermally resistive than the others with a thermal resistance of 0.012 $m^2 K W^{-1}$. The thermal resistances of Schwarz D and Gyroid structures were also assessed experimentally without electrolyte and the results are compared to numerical predictions in a previous MS thesis.

ACKNOWLEDGMENTS

My first and foremost thanks goes to Dr. Phelan for his guidance, feedback, and for providing the opportunity to work on this project. I would like to extend my gratitude to Dr. Ryan Milcarek, Dr. Dhruv Bhate for availing themselves to be part of my committee team.

Special thanks to Hooman Daghooghi Mobarakeh and Ahmad Bamasag for there to help wherever I needed it. I also want to acknowledge Benjamin Obeng for helping with models for the triply periodic minimal surface structures.

TABLE OF CONTENTS

Page

CHAPTER Page

CHAPTER Page

LIST OF TABLES

Table Page

Table Page

LIST OF FIGURES

Figure Page

Figure Page

Figure Page

Chapter 1

INTRODUCTION

Waste heat energy conversion remains a fascinating subject for research, given the renewed emphasis on energy efficiency and carbon emissions reduction. According to the Lawrence Livermore National Laboratory in 2018, 68.5% of the energy generated from all sources is rejected and thus is dissipated to the ambient environment through waste heat [1]. Moreover, a vast amount of these wastes is available from industries [2], automobiles [3], as well as buildings [4], etc. Just in 2018, buildings – both residential and commercial -- constituted about 40% of energy consumption in the US and this is projected to increase by 50% by 2050 [5]. HVAC remains the majority use of this energy. The presence of huge amounts of waste heat and the constant demand for electric energy makes this a considerable research topic. Yet, at present, there is no commercially viable technology to harness the inherent energy resource provided by the temperature differential between the inside and outside of buildings. In a geographical jurisdiction, say Phoenix, especially in the summer, much energy is used to cool and maintain the temperature in a building hence creating a huge temperature gradient between the outside and inside of the building. This resource can be tapped to generate electricity to power light bulbs or small electronic gadgets. The main project objective is to develop and analyze structural thermogalvanic modules with triply periodic minimal surface (TPMS) structures that generate electricity from the temperature gradient in building envelopes and thereby promote sustainability and electric power generation.

Amidst the various applications of TPMS across the range of fields, such as medical – due to the biomorphic design and interconnected high porosity [6], lightweighting, heat exchangers, acoustic and vibrational damping [7], energy absorption [8], among others, also of interest is their application in electric power generation. Little has been explored when it comes to their use in power generation. The complex nature of these structures, coupled with their thermal and structural properties, make this application possible, thus ensuring a high temperature gradient. In this work, lattices based on TPMS were produced using additive manufacturing and examined experimentally. This investigation elucidates their thermal resistances, which in turn helps to appreciate the power output associated with the thermogalvanic structure. Only a few of these lattice structures were examined based on the power density results from previous work [9].

1.1. Motivation

In 2018, according to the International Energy Agency, worldwide energy demand grew by 2.3% from the previous year, representing twice the growth rate since 2010. In essence, global energy-related CO_2 emissions rose by 1.7% (33 Gigatonnes), hitting a new record. Between 2018 and 2050, these figures are projected to grow by nearly 50% [5]. This necessitates research into new low-grade energy conversion technologies as an alternative source of electricity. Besides, industrial processes and electric power plants generate volumes of this excess heat; researchers all over have spent decades exploring ways to harness some of this wasted heat. However, much of these efforts were focused on thermoelectric devices, solid-state materials that can produce electricity from a temperature gradient, but their efficiency is limited by the availability of materials [10]. In this project,

we seek to bridge the gap by developing a thermogalvanic cell in the form of a robust brick that can be used as building blocks in future smart buildings to enhance sustainability and efficiency. This brick mimics the operation of a thermogalvanic cell to convert the temperature differential between the interior and exterior of buildings to generate electricity. From equation 1.1 below, it is apparent that optimizing the thermogalvanic brick to be thermally resistive while reducing the internal resistances to allow ionic transport should be the primary focus in delivering optimal power output. However, we first need to have an idea of which of the TPMS structure gives the optimum thermal resistance:

$$\eta = \frac{\alpha^2 R_{th} \Delta T}{4 R_{int}} \tag{1.1}$$

where η is the power efficiency, α the Seebeck coefficient, R_{th} the thermal resistance, R_{int} ionic resistance and ΔT is temperature difference.

1.2. Research Goal

This project encompasses several concentrations which include power output, TPMS optimization, 3D printing, thermal performance, etc., however, the main focus of this thesis is the thermal resistance of the TPMS structures in the brick.

1.3. Thermogalvanic Cell

Since the introduction of the thermogalvanic cell in 1825 [11], research studies on the topic have shown optimistic results in the past decades [12]. In the past two decades, research on them has been motivated by their potential to convert low-grade thermal energy

to electricity. According to Quickenden and Mua, studies on thermogalvanic cells (TGCs) were for two main reasons: First, the operation of the thermogalvanic cell is poorly understood. Secondly, the studies relate unconventional transducers of solar energy to electrical energy [10]. The conversion of the heat energy directly into electricity, or the reverse, by a thermoelectric device is related to electron transport phenomena, and the interrelated Seebeck, Thomson effects and Peltier effects. In the same way, thermogalvanic devices convert low-temperature waste heat into electricity through a thermogalvanic effect. One of the earliest experiments was carried out using a cell with copper (Cu) electrodes immersed in a $CuSO_4$ aqueous solution. Figure 1.1 shows a schematic diagram of TGCs using aqueous Cu.

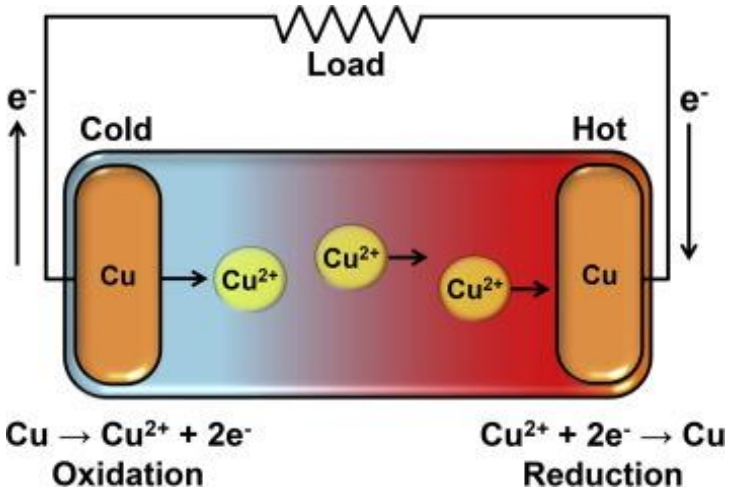

Figure 1.1. Copper Oxidation [12]

A thermogalvanic cell is a non-isothermal electro-chemical cell in which the two electrodes are deliberately held at different temperatures. The temperature difference generates a potential difference. As shown in figure 1.1, if these electrodes are connected

to a load, power can be delivered. The temperature difference between the cold and the hot electrodes creates a difference in electrochemical potential equilibrium of the redox couple on the electrodes; the cold electrode transfers Cu^{2+} to the hot electrode [12],

$$Cu \rightarrow Cu^{2+} + e^{-} \tag{1.2}$$

and the reduction of Cu^{2+} cations on the hot electrode (cathode) ensues:

$$Cu^{2+} + 2e^{-} \rightarrow Cu \tag{1.3}$$

so that electrical current and power can be delivered, thus converting thermal energy into electrical energy. The ion transport within the cell configuration is a complex combination of natural convection, migration, thermal, and chemical diffusion [13]. The temperature dependence of the electrode potential is referred to as the Seebeck coefficient (S_e), which is a measure of the magnitude of an induced thermoelectric voltage in response to a temperature difference across that material:

$$s_e = \frac{\Delta E}{\Delta T} = \frac{\Delta S}{nF}, \tag{1.4}$$

where ΔE is the open-circuit voltage, ΔT the temperature gradient, n the number of electrons transferred in the redox reaction, F Faraday's constant, and ΔS the partial molar entropy difference of the redox couple. The performance of thermogalvanic cells depends not only on the Seebeck coefficient but also on the internal and thermal resistances of the cell [14]. The efficiency of thermogalvanic cells is largely limited by the competition between thermal resistance and electrical conductance. Different methods have been explored to reduce the internal resistance with the aim of increasing the power output of the cell. This was done by reducing the length or distance between the electrodes [14].

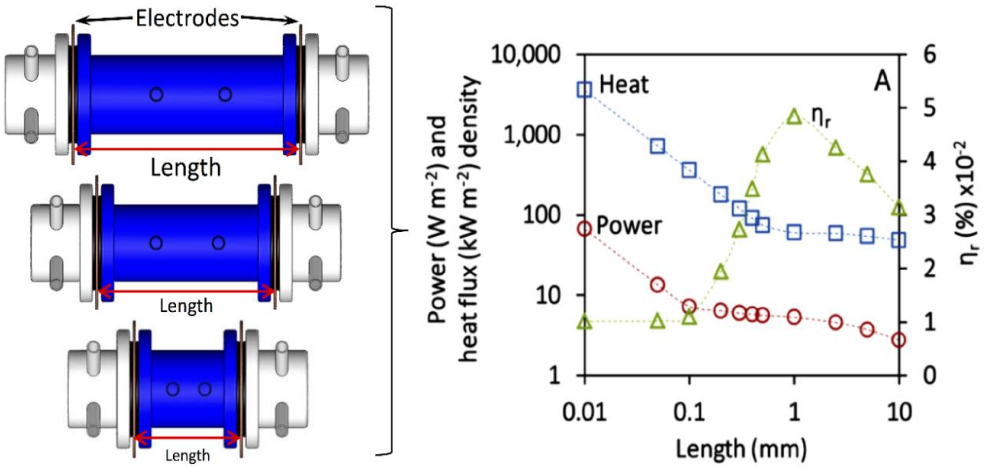

Figure 1.2. Effect of Electrode Length Eduction [14]

However, the action also reduces the thermal resistance, which increases the heat flux across the cell and ultimately lowers the power conversion efficiency of the cell, as shown on the right of figure 1.2. The power conversion efficiency, η, is defined as [15]

$$\eta = \frac{electrical\ output\ power}{thermal\ power\ flowing\ through\ cell}\ , \tag{1.5}$$

From research, it has been shown that a gelled electrolyte through the addition of some kind of powder can have considerably higher power output than using a pure electrolyte [16]. The electrode material with polarization, high charge capacity, low specific heat, high thermal resistance, etc., positively affects the efficiency of the heat-to-electric energy conversion [17]. In a recent research advancement, a new TGC was introduced that can produce a power density as high as 4 W m $^{-2}$ at a temperature difference of 30 K. Here, they replaced the traditional liquid-based redox and a single-phase mass transport with an internal gas/liquid two-phase system [18].

1.4. Triply Periodic Minimal Surface Structures

A minimal surface, mathematically, can be defined as a surface with a zero-mean curvature, that is, the sum of the principal curvatures at each point say, x_0, y_0, z_0 on the surface will give you zero. Particularly of interest are the minimal surfaces that repeat themselves in three dimensions, hence, triply periodic (thus, free from intersection). Like in a soap film, such shapes result in nature from an equilibrium of homogeneous tension. [19] [20] The first of this kind was discovered by a German mathematician named Hermann Schwarz in 1856. It was named a 'D-surface' because of its similarity to the "Diamond" network. Schwarz was able to obtain an analytical expression for the D and P-surfaces by the application of the Weierstrass formula. The Enneper-Weierstrass representation of the coordinates of a minimal surface was expressed in [21] as

$$x = Ree^{i\theta} \int_{\omega_o}^{\omega} (1 - \tau^2)\, R(\tau) d\tau, \tag{1.6}$$

$$y = Ree^{i\theta} \int_{\omega_o}^{\omega} i(1 + \tau^2)\, R(\tau) d\tau, \tag{1.7}$$

$$x = Ree^{i\theta} \int_{\omega_o}^{\omega} 2\tau\, R(\tau) d\tau, \tag{1.8}$$

where i^2 = -1 and $\tau = \tau_a + i\tau_b$, associated with the function $R(\tau)$ called the Weierstrass function, and θ is the Bonnet angle. By integration of the Weierstrass function, we can

determine a specific minimal surface. Schwarz did this to find mathematical expressions for the Schwarz D and P geometries. Schoen, later in the 1960s, discovered several types and varieties of the embedded TPMS after being entrusted by NASA to investigate the application of these geometries in space structures [19].

By a computational method, we can mathematically define the cell structures of this TPMS just by manipulating the cell size and volume fraction. A key challenge facing the designer of a lattice structure for a specific application is that of choosing the appropriate lattice design variables, that is, the cell type, cell size, volume fraction, the lattice material, etc. All these properties play crucial roles in determining the structural stiffness and strength; the same is true for thermal applications [6]. TPMS can be implicitly defined by the function

$$f(x, y, z) = t \tag{1.9}$$

where 't' is the isovalue that governs the offset from the level-set (i.e. when the function value equals zero). With arbitrary numbers of cells and volume fractions, the isosurface of the TPMS structures; Schwarz D (U_D), Schwarz P (U_P), Gyroid (U_G), Split P (U_S), and IWP (U_I) can be generated by finding the U=0 equations: [7] [22] [23]

$$Up = cos(k_x x) + cos(k_y y) + cos(k_z z) - t, \tag{1.10}$$

$$U_D = \sin(k_x x)\sin(k_y y)\sin(k_z z) + \sin(k_x x)\cos(k_y y)\cos(k_z z) + \cos(k_x x)\cos(k_y y)\sin(k_z z) - t, \quad (1.11)$$

$$U_G = \cos(k_x x)\sin(k_y y) + \cos(k_y y)\sin(k_z z) + \cos(k_z z)\sin(k_x x) - t, \quad (1.12)$$

$$U_S = 1.1(\sin(2k_x x)\cos(k_y y)\sin(k_z z) + \sin(2k_y y)\cos(k_z z)\sin(k_x x) + \sin 2z\cos(k_x x)\sin(k_y y)) - 0.5(\cos(2k_x x)\cos(2k_y y) + \cos(2k_y y)\cos(2k_z z) + \cos(2k_z z)\cos(2k_x x) - t, \quad (1.13)$$

$$U_I = \cos(k_x x)\cos y + \cos y \cos z + \cos z \cos(k_x x) - \cos(k_x x)\cos y \cos z - t, \quad (1.14)$$

where k_i is the TPMS function periodicities, defined by

$$k_i = 2\pi\frac{n_i}{L_i} \text{ (with } I = x, y, z), \quad (1.15)$$

and n_i are the numbers of cell repetitions in the *x*, *y* and *z* directions, and L_i are the absolute sizes of the structure in those directions. Using computer software, these structures can be

generated from the equations that implicitly describe them mathematically, as shown in the equations above.

Several software packages can be used in generating these structures: MathMod, Rhino with grasshopper plugin, Surface Evolver – one of the oldest, among others. However, for the purposes of this work, a software called Flatt Pack (see figure 1.3) was used in modeling these structures [7]. It was created by the University of Nottingham, not yet available commercially but upon request. Figure 1.3 shows the interface of the software, dimension, and number of unit cells used in creating 3D CAD models of the TPMS structures.

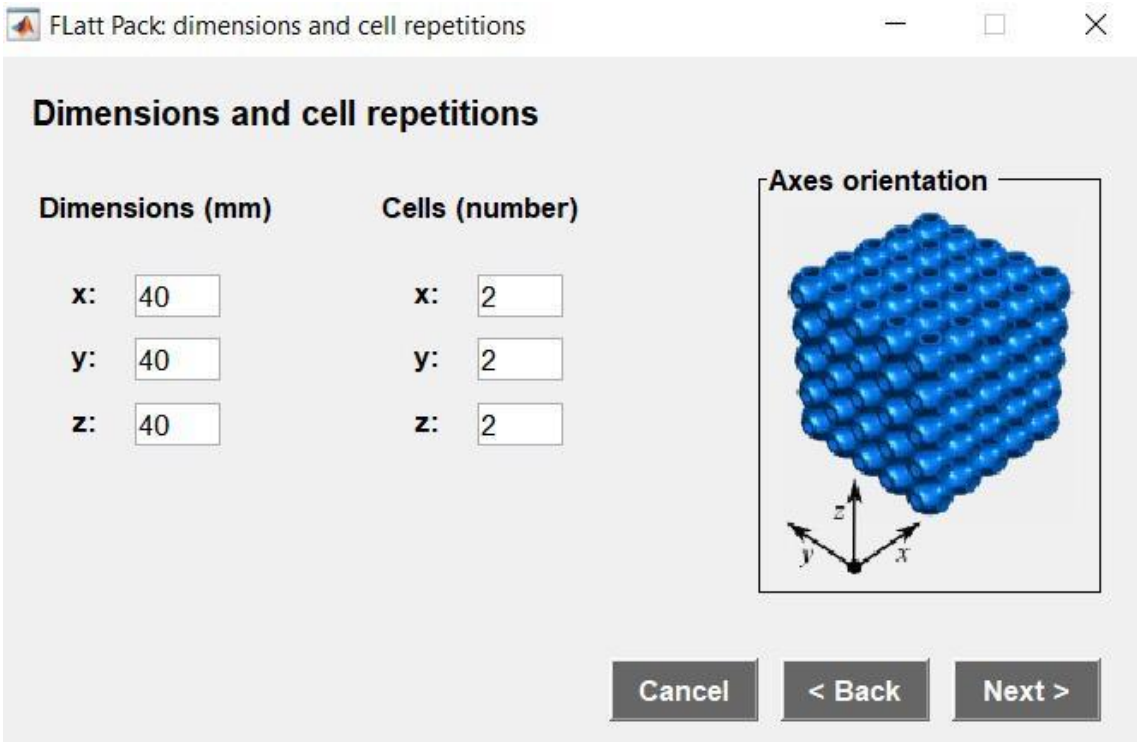

Figure 1.3. Flatt Pack Interface with Schwarz P Geometry, the Dimensions, and the Unit Cell Number [7].

1.5. Additive Manufacturing

The idea of being able to create custom product parts and the ability to fabricate structures of precise geometries as and when they are needed, has caught the attention of the general public. Additive manufacturing, as its name sounds, is the process of building a three–dimensional object by successively adding material layer by layer from a computer-aided design model. It is becoming an increasingly popular technology primarily because of its application in several fields; in the medical field [24], in the construction industry [25], and in the automobile industry [26], among several. Several types of this manufacturing method are now common, ranging from fused deposition modeling (FDM), stereolithography (SLA), selective laser sintering (SLS), etc. For the purpose of this research, the SLA method of 3-D printing was utilized for printing the TPMS lattice structures. This process is known as the first rapid prototyping method that came to the market after Charles Hull patented the first SLA process in the year 1986 as the first-ever device of its kind to print a real physical part from a computer-generated file [27]. The word stereo means three-dimensional and lithography – printing with the light; hence, the term "stereolithography was coined by him in his patent application [27].

In the SLA process, a photopolymer or light-activated resin is a polymer that changes its properties when exposed to light, often in the ultraviolet or visible region of the electromagnetic spectrum as shown in figure 1.4. These changes are often manifested structurally, for example hardening of the material occurs as a result of cross-linking when exposed to light [28].

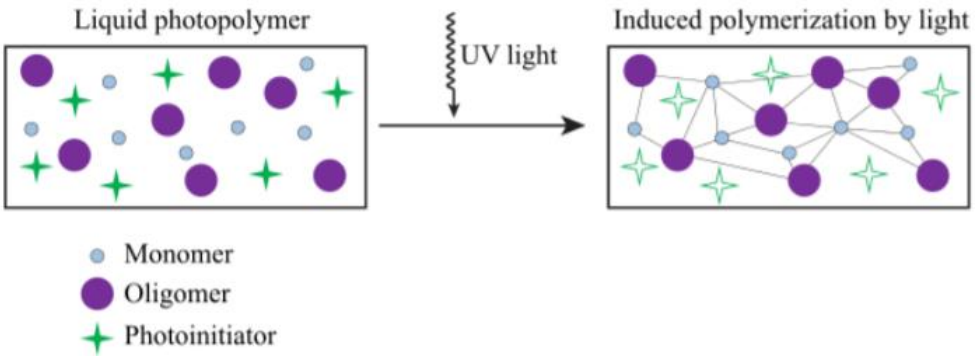

Figure 1.4. Polymerization of Liquid Photopolymer when Exposed to UV light [29].

Through the process of curing, monomers, oligomers, and photo-initiators conform into a hardened polymeric material [28]. The liquid resin is cured layer by layer. After a layer is patterned with exposure of UV light through a transparent plate such as in LCD printers, the cured structure is detached from the transparent plate. It is then raised to allow uncured resin to fill the space between the transparent film and structure. The next layer is then ready to be patterned. The process of printing can vary; bottom-up, thus, unlike the fused deposition method, it prints in the reverse direction. Figure 1.5 shows the printing process.

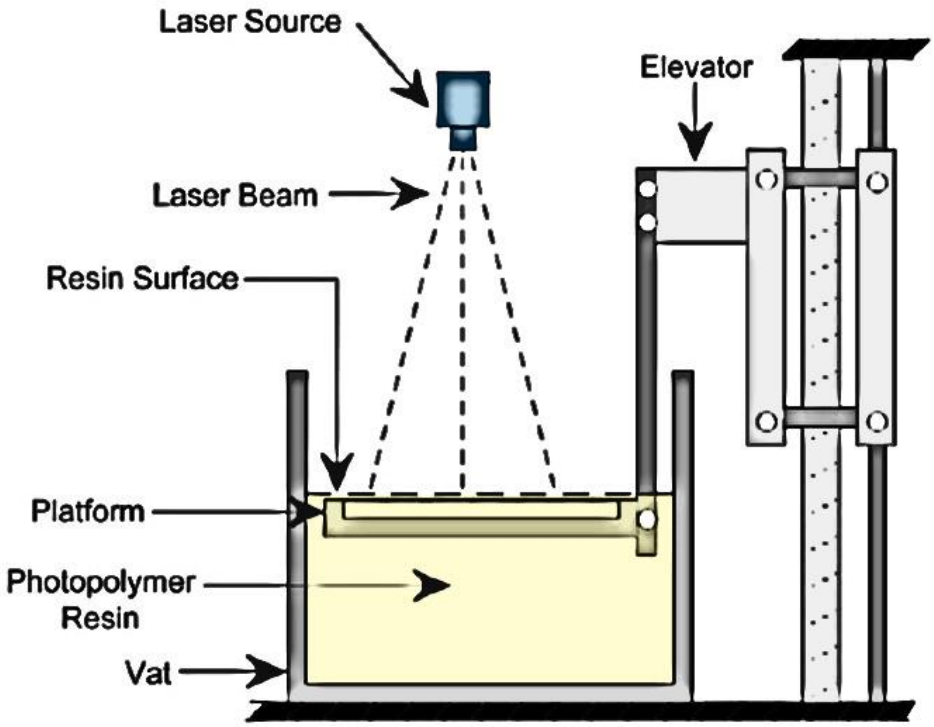

Figure 1.5. SLA Printing Process [30]

There are several advantages associated with SLA 3D printing. The printing time is reduced as compared to the FDM process, yet a high fabrication accuracy is maintained and has a higher resolution – as high as 0.05mm. One does not require support material except for complex overhanging objects. The photopolymer materials used can either be Acrylonitrile butadiene styrene (ABS) polymer or Polylactic acid (PLA) polymer. One layer is solidified at a time on the surface of the resin giving rise to a shorter printing time. Figures 1.7 and 1.8 show the 3D-printed samples with the manufacturing process.

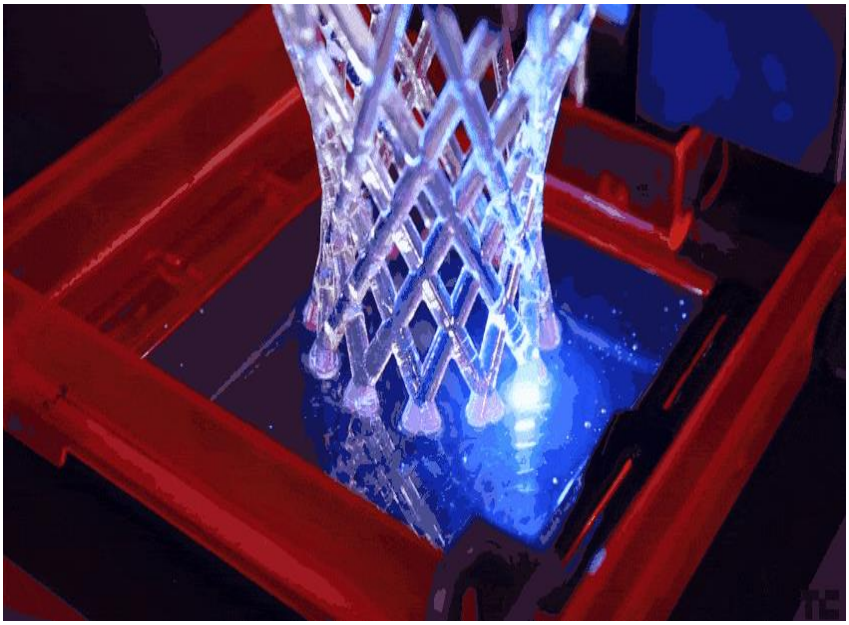

Figure 1.6. SLA Printer (Projection-Based Printing)

Figure 1.7. 40 x 40 x 40 *mm* 3-D Printed IWP Lattice Structure

(a)

(b)

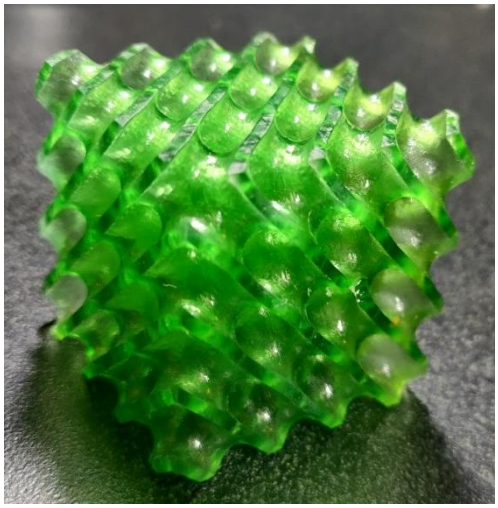

(c)

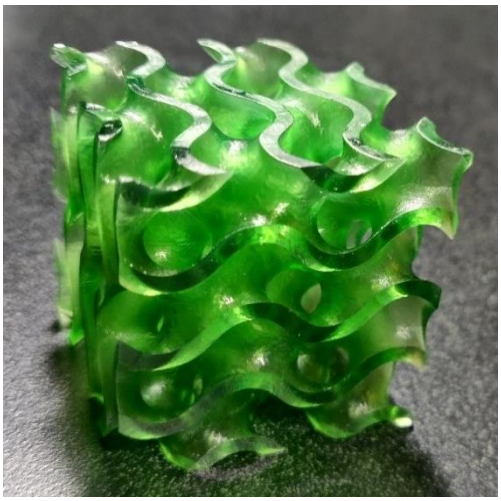

(d)

Figure 1.8. 40 x 40 x 40 *mm* 3-D printed TPMS Lattice Structures with SLA Printer: (a) - Schwarz P, (b) - Split P, (c) - Schwarz D, (d) - Gyroid.

Chapter 2

THEORY

Several fundamental principles govern the thermogalvanic brick system mainly because of the coalescence of thermal, chemical, electrical, and mechanical properties. In this study, the primary focus is on thermal properties, thus heat transfer, thermal resistance, etc. Even more so of importance to thermogalvanic cells is the Seebeck coefficient. From previous studies, 0.7 M $CuSO_4$ + 0.1 M H_2SO_4 aqueous electrolyte gave the optimum Seebeck coefficient, therefore, it was employed for our study. [31] [32]

2.1. Rate of Heat Flow

Like in every thermogalvanic cell, the two electrodes (see figure 2.1) are held at different temperatures to establish a temperature gradient. This is achieved by passing electric current through the strip heater to heat up one of the copper electrodes (figure 2.1).

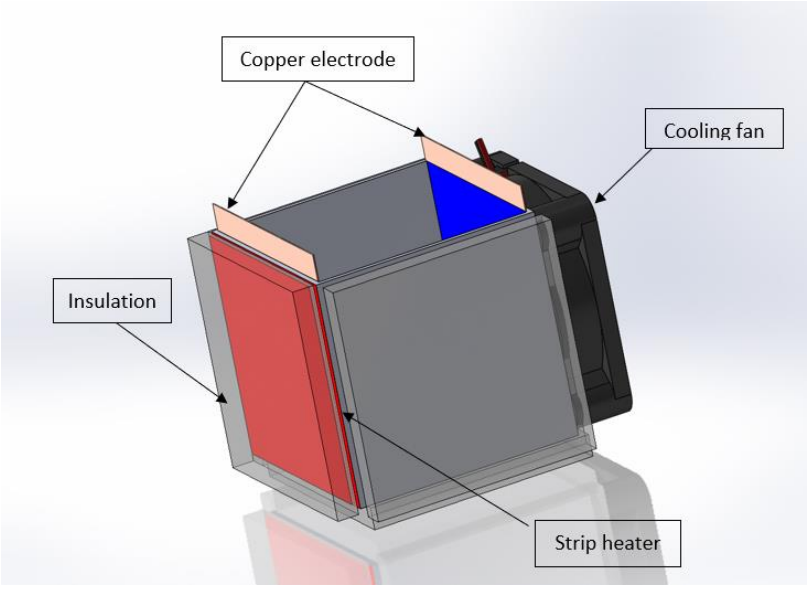

Figure 2.1. Prototype of the Thermogalvanic Brick

The rate of heat flow is given by the total electrical power entering the system through the strip heater. The power is determined from:

$$P = VI \tag{2.1}$$

and from Ohm's law

$$V = IR \tag{2.2}$$

I was determined by applying a known external resistance *R* as:

$$I = \frac{V}{R} \tag{2.3}$$

where *V* is the voltage, *I* the current flowing through the strip heater, *R* the resistance of the resistor, and *P* the power input into the system. Hence, the rate of heat flow, $\dot{Q}$, can be expressed as

$$\dot{Q} = \frac{VI}{A_{TPMS}}, \tag{2.4}$$

where A_{TPMS} is the surface area of the TPMS structures. Due to the close contact of these structures with copper electrodes, the surface area was taken as the area of the copper electrode disregarding the porosities.

2.2. Heat Flow

Conduction can take place in liquids as well as gases. The rate of heat conduction through the TPMS structure from the hot side to the cold side is proportional to the temperature difference across it and the area normal to the direction of heat transfer. This is expressed by Fourier's Law of heat conduction in a differential form for one-dimensional heat conduction as

$$\dot{Q}_{cond} = -kA\frac{dT}{dx} \tag{2.5}$$

where k is the thermal conductivity of the material, A the area and dT/dx the temperature differential. Heat is transferred in the direction of decreasing temperature, and thus the negative sign in equation 2.5 warrants that heat transfer is positive in the positive x-direction.

Equation 2.5 can be rewritten as:

$$\dot{Q}_{cond} = -kA\frac{\Delta T}{L} \tag{2.6}$$

to calculate the rate of conduction heat transfer when the thickness L of the structure or the insulation is known and ΔT is given as the temperature difference, where

$$\Delta T = T_1 - T_2. \tag{2.7}$$

Given the R-value of the insulation, R_{ins} instead, the rate of heat flow or loss can be calculated with the following equations:

$$\dot{Q}_{cond} = \frac{T_1 - T_2}{R_{ins}} \tag{2.8}$$

where

$$R_{ins} = \frac{L}{k}. \tag{2.9}$$

The rate of heat loss to the ambient was given by the net rate of heat loss through conduction, convection, and radiation. Considering the temperature T_{ins} of the insulation

surface relative to the ambient temperature (T_∞), we can calculate heat loss through convection by Newton's law of cooling expressed as

$$\dot{Q}_{conv} = hA_{ins}(T_{ins} - T_\infty) \tag{2.10}$$

where A_{ins} is the surface area of the insulation material, and h is the convective heat transfer coefficient. At higher temperatures, heat loss through radiation becomes significant; therefore, we accounted for it by

$$\dot{Q}_{rad} = \varepsilon\sigma A_s(T_s^4 - T_{surr}^4), \tag{2.11}$$

where ε is the emissivity, σ the Stefan-Boltzmann constant, A_s the surface area, T_s the temperature of the surface and T_{surr} the temperature of the surroundings.

2.3. Thermal Resistance

Using the analogy of electric current flow (I) to heat transfer, where

$$I = \frac{V_1 - V_2}{R_e}, \tag{2.12}$$

and $V_1 - V_2$ is the voltage difference across an electrical resistance, R_e, the thermal resistance (R_{TPMS}) of the TPMS lattice structure can be expressed in a similar manner as

$$R_{TPMS} = \frac{\Delta T}{\dot{Q}_{net}}. \tag{2.13}$$

$\dot{Q}_{net}$ is the net heat entering into the system, and ΔT the temperature differential measured from a differential thermocouple arrangement. Here, ΔT is comparable to the voltage difference (ΔV), the heat flow rate ($\dot{Q}_{net}$) to the current flowing through the circuit and thermal resistance (R_{TPMS}) to the electrical resistance.

2.1. One-dimensional Heat Flow

Unlike temperature, heat is a vector quantity; hence, it has both magnitude and direction. Heat transfer through a medium in most general cases is three-dimensional; however, there are a few assumptions made in this case. The electrode has a large surface area relative to its thickness and can be approximated as a large plane wall; therefore, one-dimensional heat transfer is assumed [33]. Realistically, losses occur and must be accounted for accordingly. From the first law of thermodynamics;

$$\begin{pmatrix} Total\ energy \\ entering\ the \\ system \end{pmatrix} - \begin{pmatrix} Total\ energy \\ leaving\ the \\ system \end{pmatrix} = \begin{pmatrix} Change\ in\ the \\ total\ energy\ of \\ the\ system \end{pmatrix}, \tag{2.14}$$

Considering a rate form, this can be expressed as,

$$\dot{E}_{in} - \dot{E}_{out} = dE_{system}/dt, \tag{2.15}$$

The energy change of the system does not change with time during the process; hence, the process is considered steady. E_{system} ultimately goes to zero, leaving the equation as

$$\dot{E}_{in} = \dot{E}_{out} \tag{2.16}$$

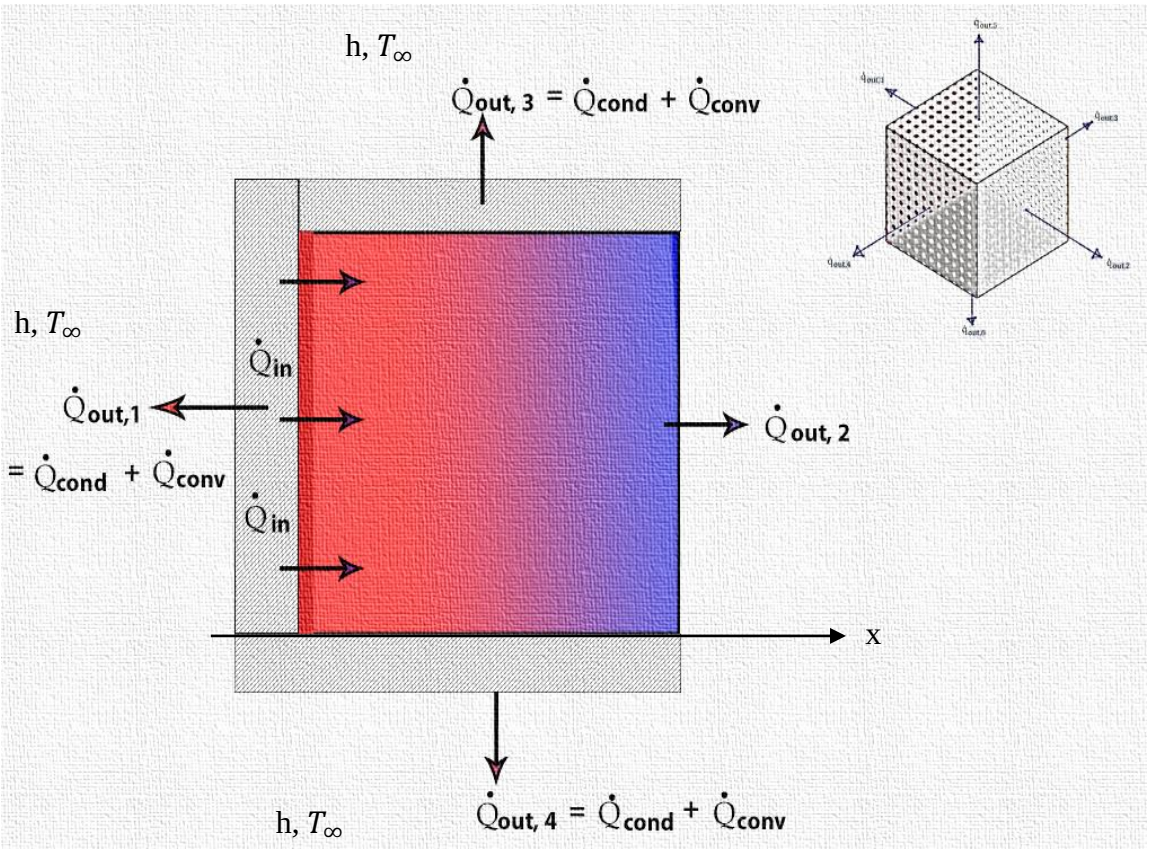

Figure 2.2. Shows how One-Dimensional Heat Flow was Estimated in the Positive *X*-Direction by Accounting for all the Heat Losses in the Different Directions

From equation (2.16), the heat entering the system is equal to the heat leaving, therefore as shown in figure 2.2, we can express the first law of thermodynamics as

$$\dot{Q}_{in} = \dot{Q}_{out,1} + \dot{Q}_{out,2} + \dot{Q}_{out,3} + \dot{Q}_{out,4} + \dot{Q}_{out,5} + \dot{Q}_{out,6}, \qquad (2.17)$$

where $\dot{Q}_{out,5}$ and $\dot{Q}_{out,6}$ are the heat losses at the top and bottom of the setup respectively (not shown in figure 2.2). The net rate of heat flowing through the system after taking out all the losses can be evaluated as

$$\dot{Q}_{net} = \dot{Q}_{in} - (\dot{Q}_{out,1} + \dot{Q}_{out,3} + \dot{Q}_{out,4} + \dot{Q}_{out,5} + \dot{Q}_{out,6}) \qquad (2.18)$$

2.2. Thermal Resistance Network

Using an elementary thermal resistance network analysis, we can better understand the thermal behavior of the TPMS lattice structure and gain insight into the experimental design, and hence how heat loss was determined.

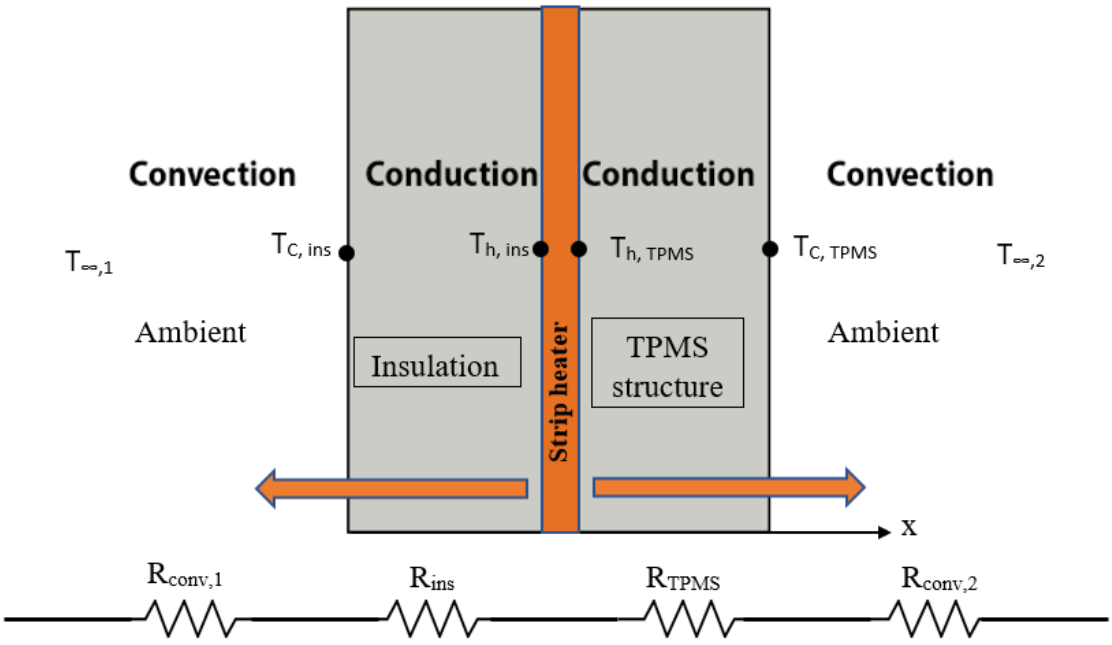

Figure 2.3. One-Dimensional Thermal Resistance Model of the Thermogalvanic Brick

As shown in figure 2.3, heat is transferred from the strip heater (T_h) through the TPMS structure to the cold electrode (T_c) through conductive resistance and to the ambient through convective resistance. However, there is a flow of heat through the thermal insulation, which should be accounted for. The total thermal resistance, hence, is expressed as;

$$R_{total} = \frac{\left(R_{conv,1} + R_{ins}\right)\left(R_{TPMS} + R_{conv,2}\right)}{\left(R_{conv,1} + R_{ins}\right) + \left(R_{TPMS} + R_{conv,2}\right)}, \quad (2.19)$$

where $R_{conv,1}$ is the thermal resistance of surface 1 with respect to heat convection (convection resistance), R_{ins} conduction resistance in the insulation, R_{TPMS} the conduction resistance in the TPMS and $R_{conv,2}$ the convection resistance of surface 2.

Chapter 3

EXPERIMENTAL DESIGN

3.1. Previous Experimental Setup

From the previous experimental setup (see figure 3.1) [9], an ASTM standard size 3D printed brick of 199 mm x 88.8 mm x 52.3 mm dimensions was used. The brick is placed in a box between the hot and cold chambers. With the help of TECs, these chambers are controlled to mimic the different temperatures that exist between the outside and inside of a building.

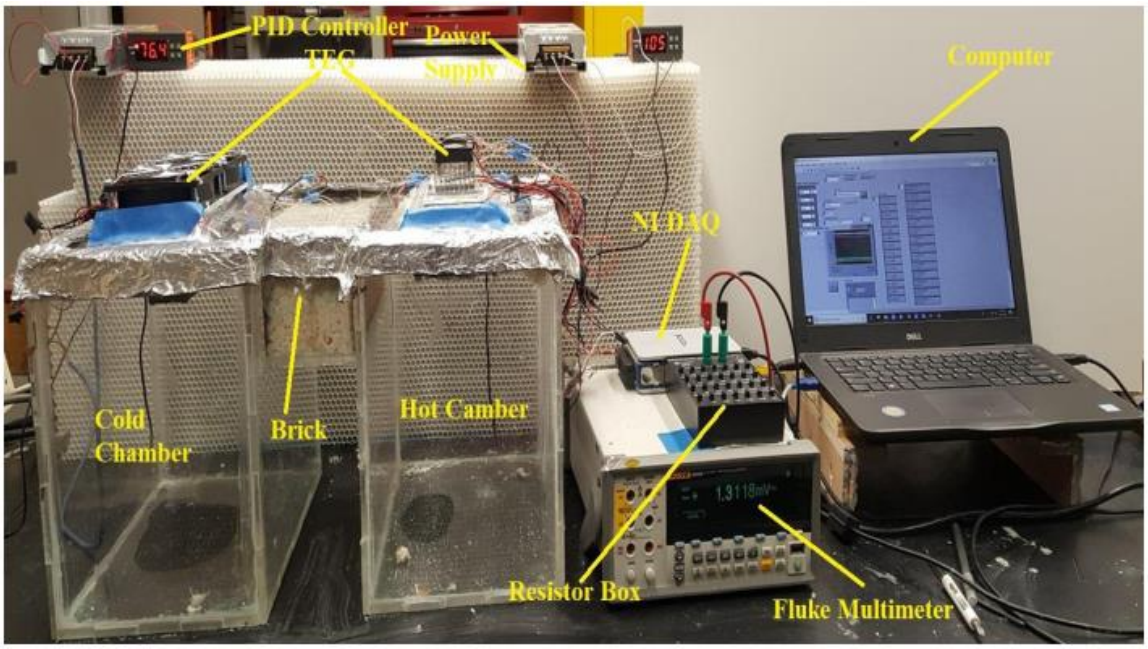

Figure 3.1. Previous Experimental Setup [9]

Nonetheless, the setup had some drawbacks; the time taken to reach steady-state when running an experiment was enormous (between 3 – 4 hours). Also, because of the size of the TPMS lattice structure utilized, it could take up to 48 hours to get one of these structures

printed, notwithstanding the queue involved because of the busy nature of the ASU Makerspace. Besides, there is a lot of material (filament) used for 3D printing. Changes were made to the setup to alleviate these drawbacks.

Furthermore, the outcome in the previous experiments performed for this project actually influenced our decision to estimate the thermal resistance of a selected few of these lattice structures. The power output for eight different 3D-printed TPMS lattice structures was tested and analyzed. In his report, he ran three sets of experiments for all eight structures. From the first experimental test, the Split-P structure was shown to have a higher maximum power density followed by the Lidinoid structure as shown in figure 3.2 [9].

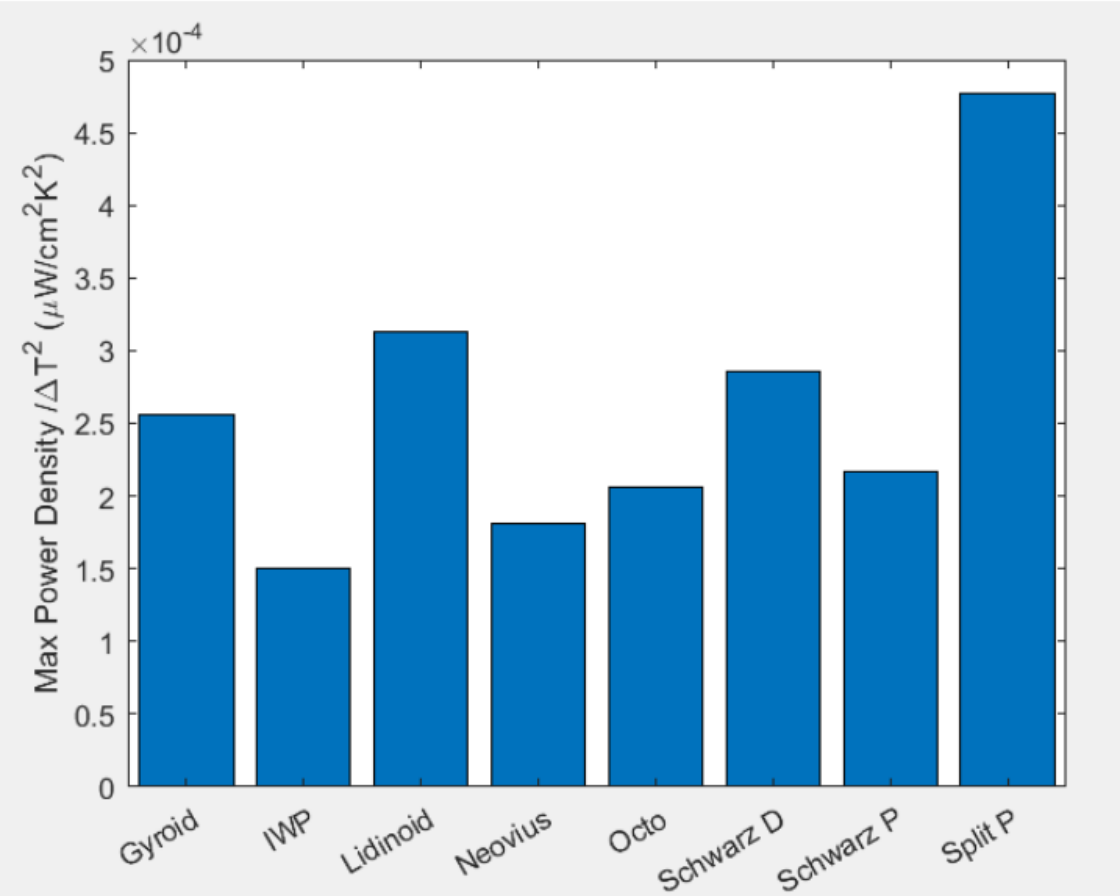

Figure 3.2. Results from the First Experimental Test [9]

However, the second test proved differently due to the discrepancies associated with reaching steady state before data logging. From the results of the second test, the gyroid and IWP structures were observed to yield higher power outputs. Although there exist some differences in the outcome of the power densities, there are some lattice structures that showed low power output in both cases. Hence, our focus was centered on the structures with relatively higher power output -- Split-P, gyroid, Schwarz-D, and IWP.

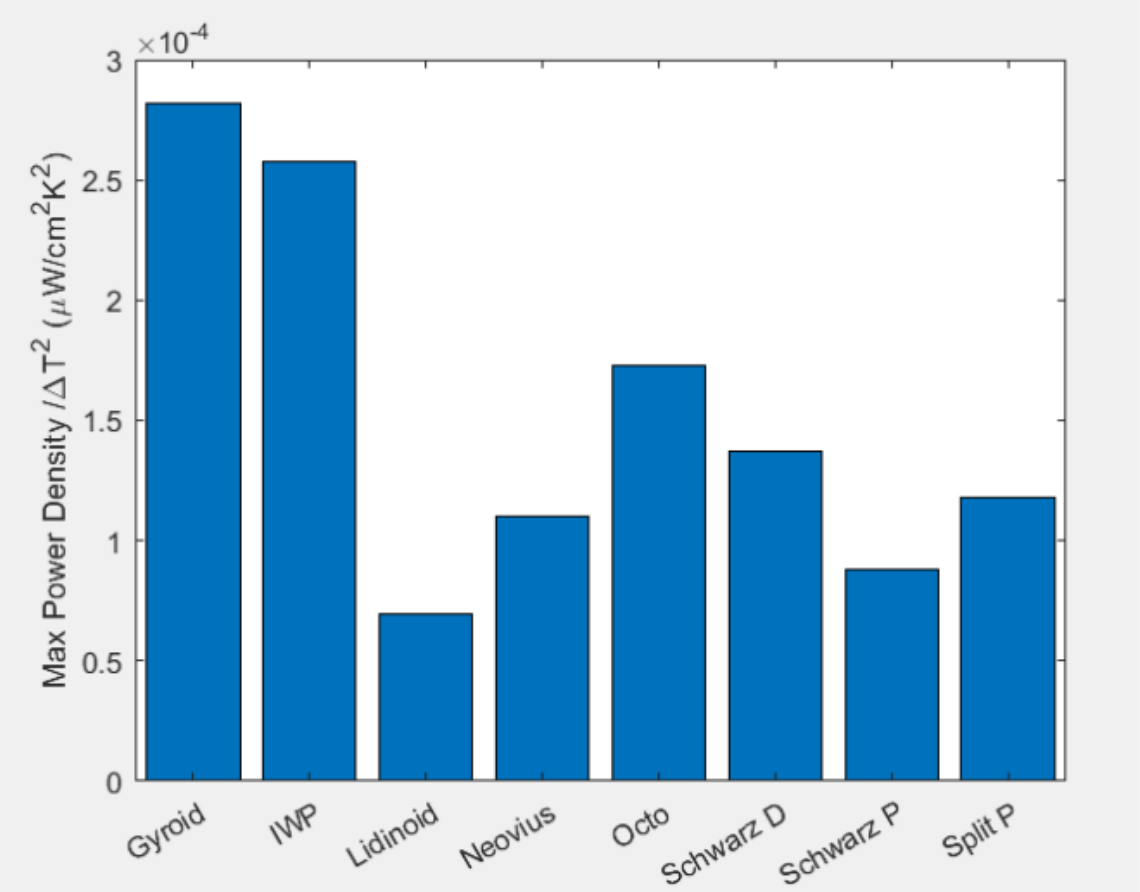

Figure 3.3. Results from the Second Experimental Test [9].

3.2. Current Prototype

The experimental setup employed in this thesis is a scaled version of the previous setup with some variations for our purpose and to ensure more accurate ΔT results. The prototype of the thermogalvanic brick (see figure 3.4) is made up of 5.6-*mm* thick acrylic casing with inside dimensions of 40 x 40 x 40 *mm*, however, two opposite sides of the cube were left open. Two cut copper electrodes of the same size were attached to the opened space of the acrylic case. Two sets of differential thermocouple circuits and conventional thermocouple configurations were soldered to the copper plate. Like shown in figure 3.4, a strip heater

was fastened to one of the copper electrodes to create the hot region and a cooling fan on the other. A 0.74 $m^2 K W^{-1}$ R-value thermal insulation of 25.4 *mm* thickness was used to insulate all surfaces but the cooling side to reduce heat loss, and also to ensure one-dimensional heat flow.

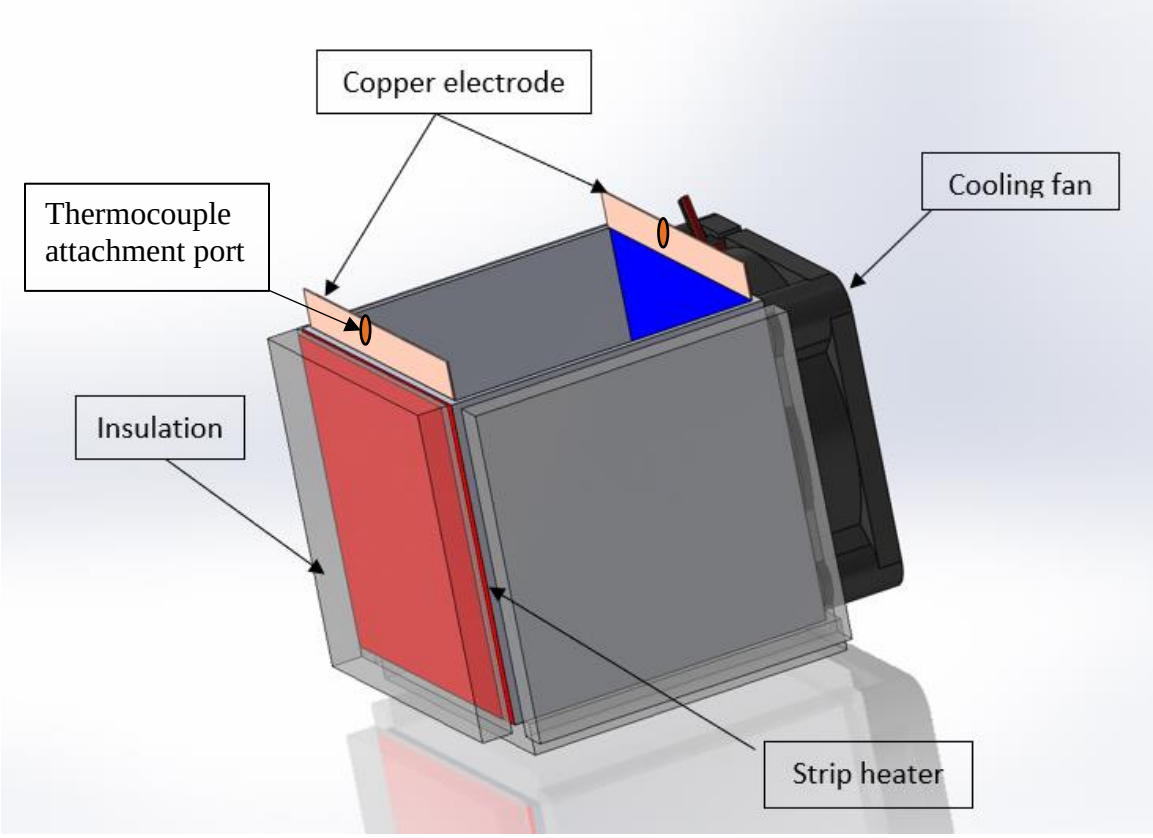

Figure 3.4. Prototype of the Thermogalvanic Designed in SolidWorks

3.3. Materials

The materials used in building the setup are found in Table 3. 1. This includes materials purchased and those already available in the lab. Table 3.2 shows the necessary equipment used in the experimental setup. The photolithograph resin used is an acrylonitrile butadiene styrene (ABS) – like photopolymer material.

Table 3.1. Table of the Bill of Materials Used in this Project

Item	Detailed Description	Supplier	Size	Qty.
Thermocouple	K Type	Omega	100 *ft, 0.4mm* diameter	1
DI Water	Deionized Water	ASU Chemistry Lab Supply	1 *gallon*	1
Copper	Pure Copper	Industrial Metal Supply	12" × 12" × 0.02362	1
Sulfuric Acid	H2SO4, ACS Grade *CAS*#7664 - 93 - 9	AMRESCO	500 *mL*	1
Copper (II) Sulfate Pentahydrate	CuSO4·5H2O 99% *CAS*#7758 - 99 - 8	PTI Process Chemicals	2.5 *kg*	1
Wire	20 Gauge	Standard	1 *m* Length	4
Beaker	Glass	Pyrex	500 *mL*	2
Graduated Cylinder	Glass	Pyrex	500 *mL*	1
Strip Heater	20 *W*	Grainger	2" × 2"	1
Acrylic Sheet	0*:*22" Thick	Home Depot	24" × 36"	1
Nitrile Gloves	Chemical Resistant	Deal Med	Standard	1
Adhesive				1
Sandpaper	220 Grit and 600 Grit	3M	Standard	1
Thermal Insulation	1 *in* Thick Minimum	Zoro	1”x48”x24”	1
3D Printing Resin	ABS-like photopolymer resin	Elegoo	1 *kg*	1
Heat Sink Compound	340 Silicone	DOW Corning	142 *g*	1

Table 3.2. Table of Equipment Needed to Perform the Experiments.

Equipment	Model	Manufacturer	Quantity
cDAQ	9171	NI	1
DAQ Thermocouple Module	9213	NI	1
Programmable DC Power Supply	PS2520G	Tektronix	3
Computer	With LabVIEW	-	1
3D Printer	LCD - SLA	Monoprice	1
Multimeter	Iensen	NI	1
Soldering gun	Weller	-	1

3.4. Actual Power Input

Since multiple power supplies were connected to provide input power for the strip heater, we need to measure the actual power input to know accurately the heat flux entering into the thermogalvanic brick system. As shown in figure 3.5, the voltage across the strip heater was measured by connecting a multimeter.

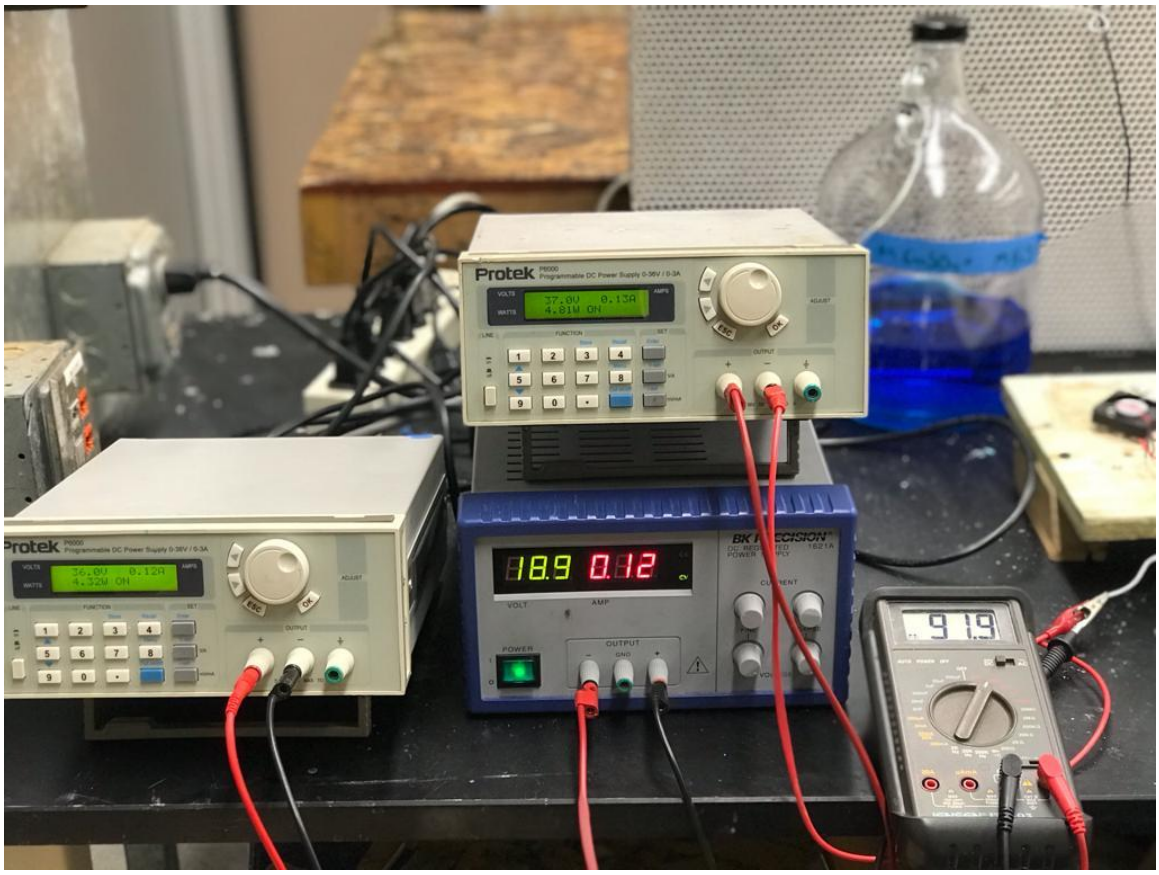

Figure 3.5. Three Programmable Power Supplies Connected in Series with a Multimeter Showing the Voltage Across the Strip Heater.

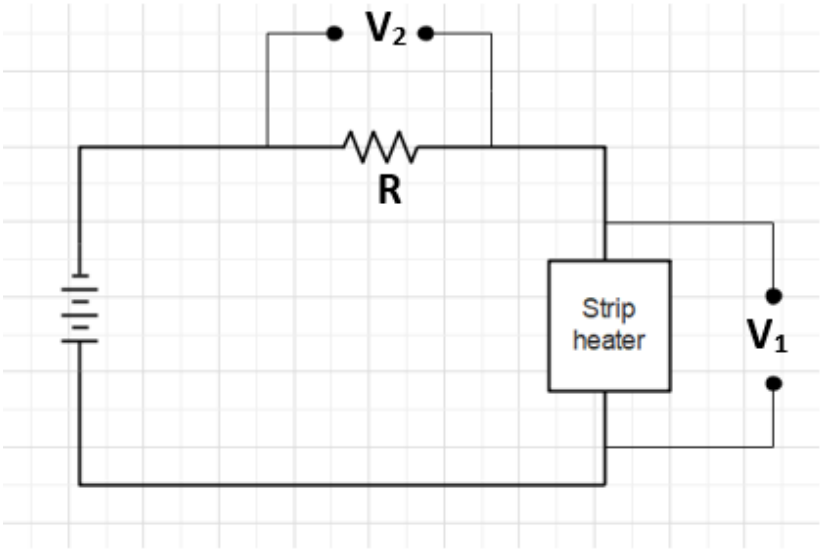

Figure 3.6. Schematic Diagram of the Circuit Showing how the Actual Current Flowing Through the System was Quantified

The precise current flowing through the strip heater was evaluated by introducing an external resistor of known resistance (see figure 3.6). Using Ohm's law (equation 2.3), we can calculate the current flowing through the system.

3.5. Differential Thermocouples

Thermocouples are one of the most used temperature measuring devices due to their being relatively inexpensive yet accurate in measurement, and they operate over a wide range of temperatures. The basis of operation of thermocouples was established by Thomas Seebeck in 1821 when he discovered that voltage is generated by conductor subjected to a temperature difference [34].

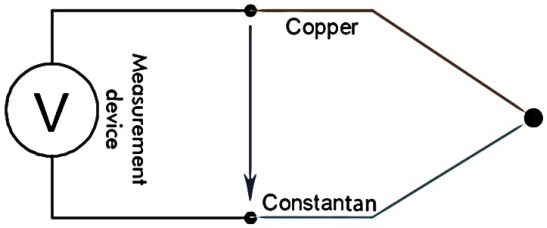

Figure 3.7. Image of the Schematics of a Thermocouple

As shown in figure 3.7, the voltage generation requires two dissimilar conductors of different electrical properties to produce the thermoelectric effect. From the Seebeck effect, the voltage (V) induced proportionally to the temperature gradient (ΔT) can be expressed as

$$V = S\Delta T, \tag{3.1}$$

where S is the Seebeck coefficient (thermoelectric power, or thermopower, in V/K). Traditionally, measuring the ΔT of two surfaces with a thermocouple means the difference of temperature measurement at the hot and cold side of the surfaces like shown in figure 3.8.

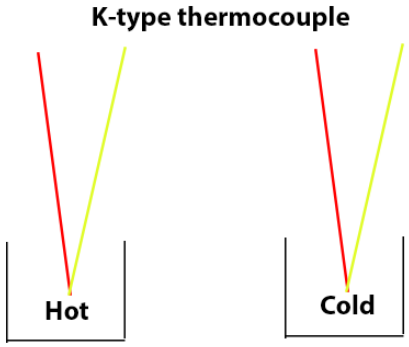

Figure 3.8. Traditional Thermocouple Arrangement

Hence, the combined limits of error for the ΔT is the square root of the sum of the squares of the individual thermocouple limits of error. Thus, the uncertainty, $U_{\Delta T}$, associated with a calculated ΔT for a conventional thermocouple arrangement is expressed as

$$U_{\Delta T} = \sqrt{{U_{T_1}}^2 + {U_{T_2}}^2}, \tag{3.2}$$

$$U_{\Delta T} = \sqrt{2}\, U_T \tag{3.3}$$

The coefficient, $\sqrt{2}$ of U_{T_1}, however, can be eliminated when we employ a differential thermocouple configuration. In configuring the thermocouple to measure temperature differentially, either the positive or negative legs of the thermocouple are connected and attached to the hot and cold sides of the surface. As shown in figure 3.9, the remaining legs of the thermocouple (either wire) are connected to the DAQ.

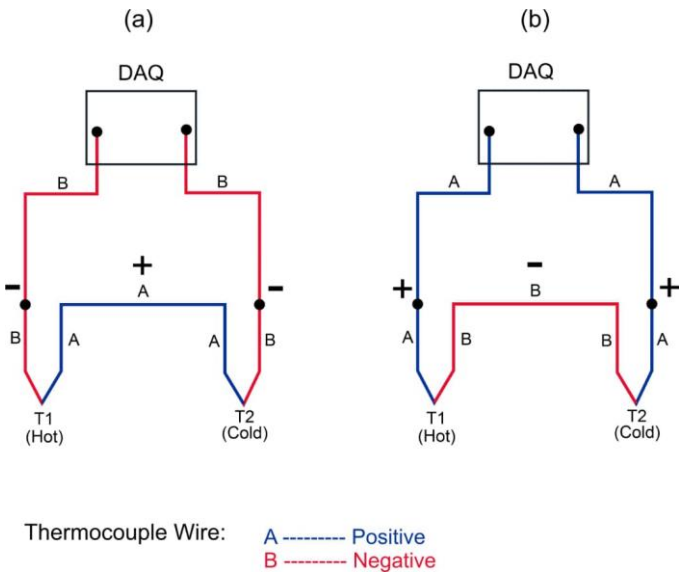

Figure 3.9. Differential Thermocouple Configuration

Although several types of thermocouples are available for various reasons, for the purposes of this work, the K-type was utilized. Configuration (a) or (b) (figure 3.9) can be used in the differential temperature measurement; however, our experimental tests proved (a) to be more accurate, that is, configuration (a) led to an accuracy of ± 0.2℃ whereas (b) gave ±0.9℃ accuracy. Hence, figure 3.10 is considered the more accurate arrangement and the one which was followed in subsequent experiments.

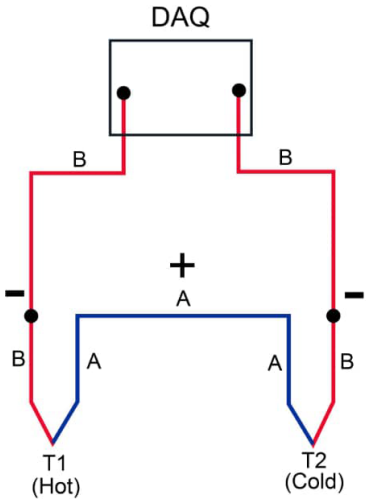

Figure 3.10. Preferred Configuration

Changing the junction of the thermocouple in relation to the hot and cold side of the configuration only results in the reversal of the polarity of the ΔT signal. The thermocouple data acquisition device was calibrated using a Plolystat Standard 3-6L Heat/Cool Bath with an accuracy of ±0.05 ℃ and an ice bath kept at zero degrees. A polynomial function $\Delta T = V/41\mu V$℃ of thermoelectric voltage, V (μV) as a function of temperature, ΔT (℃) was obtained and double checked with the tables from the National Institute of Standards and Technology (NIST).

Figure 3.11. An image of the Thermocouple Calibration

One junction was inserted into the ice bath at zero degrees and the other end in the thermal bath as shown in figure 3.11. When both legs are placed in the ice bath, the outcome is seen in figure 3.12. This shows a measured error of about ±0.2℃ (see figure 3.12).

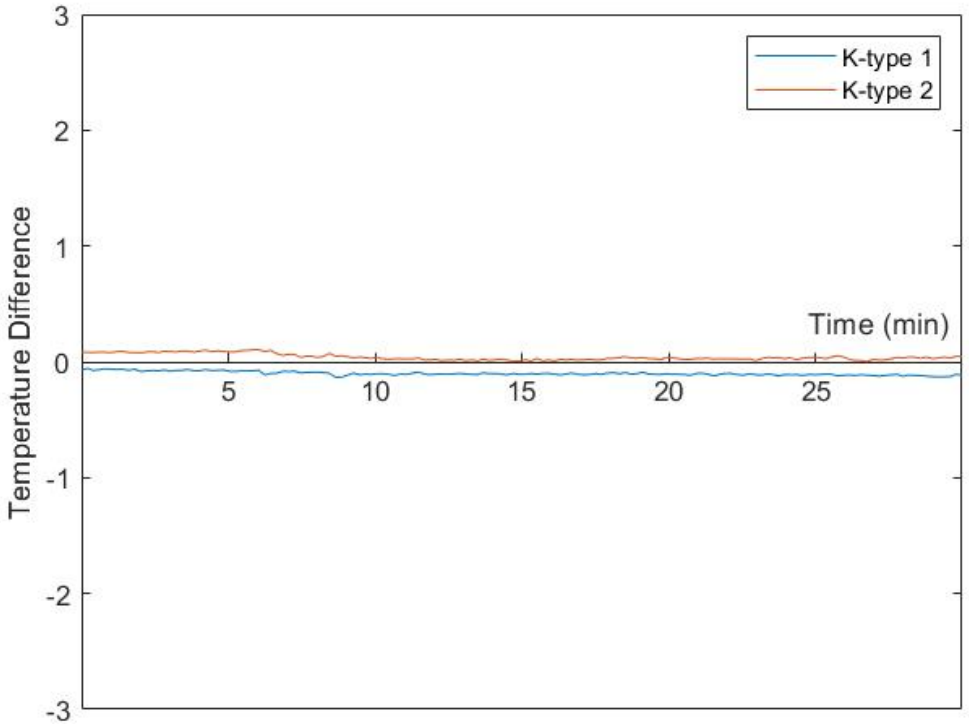

Figure 3.12. A Plot of ΔT for Two Different K-Type Differential Thermocouple at 0°C

3.6. Area of Cross Section

The architecture of the TPMS structures (figure 1.8) is a complicated one, hence, measuring the cross-sectional area conventionally is not possible. To calculate the area, the models were imported into Autodesk additive manufacturing called Autodesk Netfabb, and were sliced $1/10^{th}$ of a mm, that is, 400 images for a 40 mm high model. These images were exported as .BMP files.

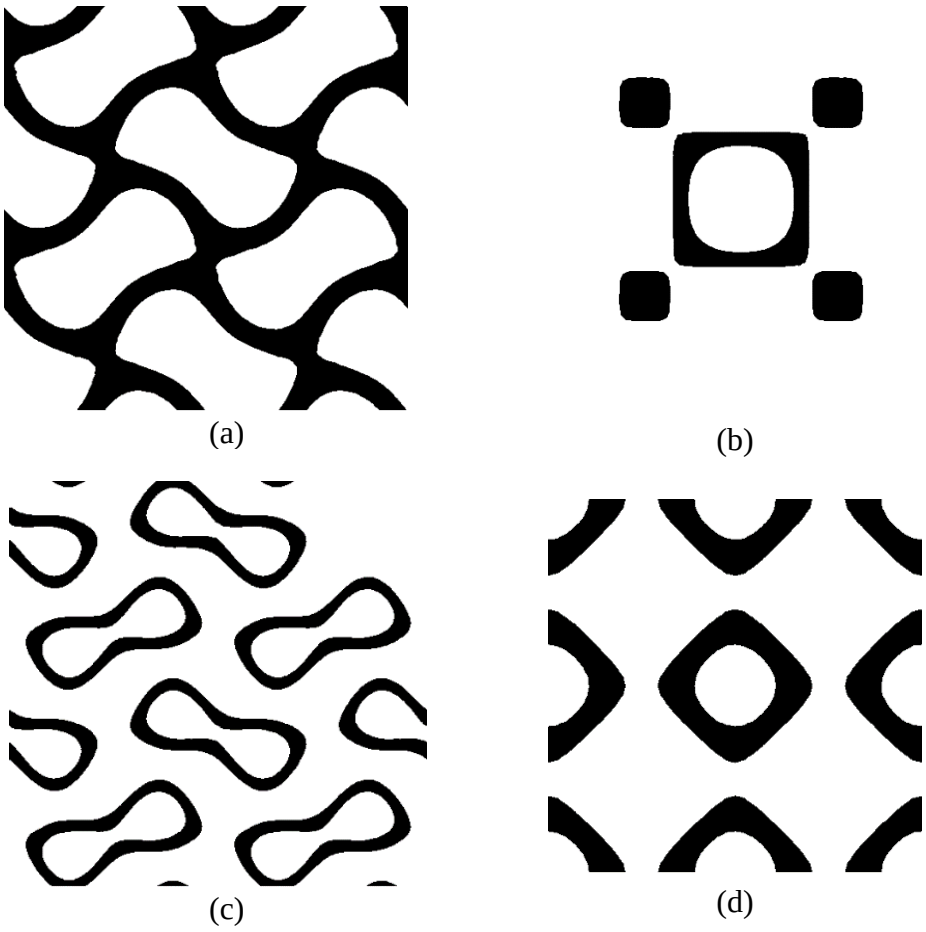

Figure 3.13. Sliced Images of the TPMS Modelled as Exported from Autodesk in MATLAB (a) - Gyroid, (b) - IWP, (c) - Split P, (d) - Schwarz P.

The .BMP files were imported in MATLAB and the images (figure 3.13) were analyzed. The black shade in figure 3.13 images is the solid area and white is the void in the TPMS structures. The images can be analyzed in MATLAB as binaries; 0 as black and 1 as white, hence, the percentage of black area can be evaluated by measuring the pixels that are black (see Appendix A). Since the cross section of the structures varies layer by layer, the average of the percentage black was calculated and then multiplied by the area of the image (40mm x 40mm) to find the average cross-sectional area of the TPMS model (see table 3.3).

Table 3.3. Cross Sectional Area of the Developed TPMS Models Calculated Using the MATLAB Code.

Model	Percentage of Black	Cross-sectional Area (mm^2)
Split P	0.1228	196.4461
IWP	0.0693	110.9285
Schwarz Primitive	0.1803	288.4649
Gyroid	0.1055	168.8709

Chapter 4

EXPERIMENTAL PROCEDURE

In this chapter, the various procedures followed in performing the experiments will be highlighted. This includes the electrolyte preparation.

4.1. Electrolyte Preparation

From previous work [14] [32], an optimum concentration of the copper sulfate pentahydrate was determined as 0.7 M $CuSO_4$ + 0.1 M H_2SO_4. Here, the correct mass of $CuSO_4 \cdot 5H_2O$ salt crystals is dissolved in deionized water to about 80% of the final volume to form an aqueous electrolyte solution. After, we add sulphuric acid (ACS grade H_2SO_4) to the solution. More deionized water is added to the solution to yield the correct volume and consequently the correct concentration. At this point, the solution is often cloudy due to incompletely dissolved crystals. The solution is stirred until everything is completely dissolved. This may take several minutes. Since the setup is a scaled version of the original brick size, a 500mL batch of electrolyte is sufficient to perform all the tests.

4.2. Experimental Setup

As shown in figure 4.1, a 40 x 40 x 40 *mm* acrylic box is laser-cut, and a copper plate fastened on opposite ends of the acrylic with an adhesive to ensure the electrolyte is securely contained. Following the differential thermocouple arrangement explained earlier, the Omega K-type thermocouples are soldered to the copper electrode, two per side. This is done to alleviate discrepancies in temperature measurement associated with loose contact with the electrode in previous experiments.

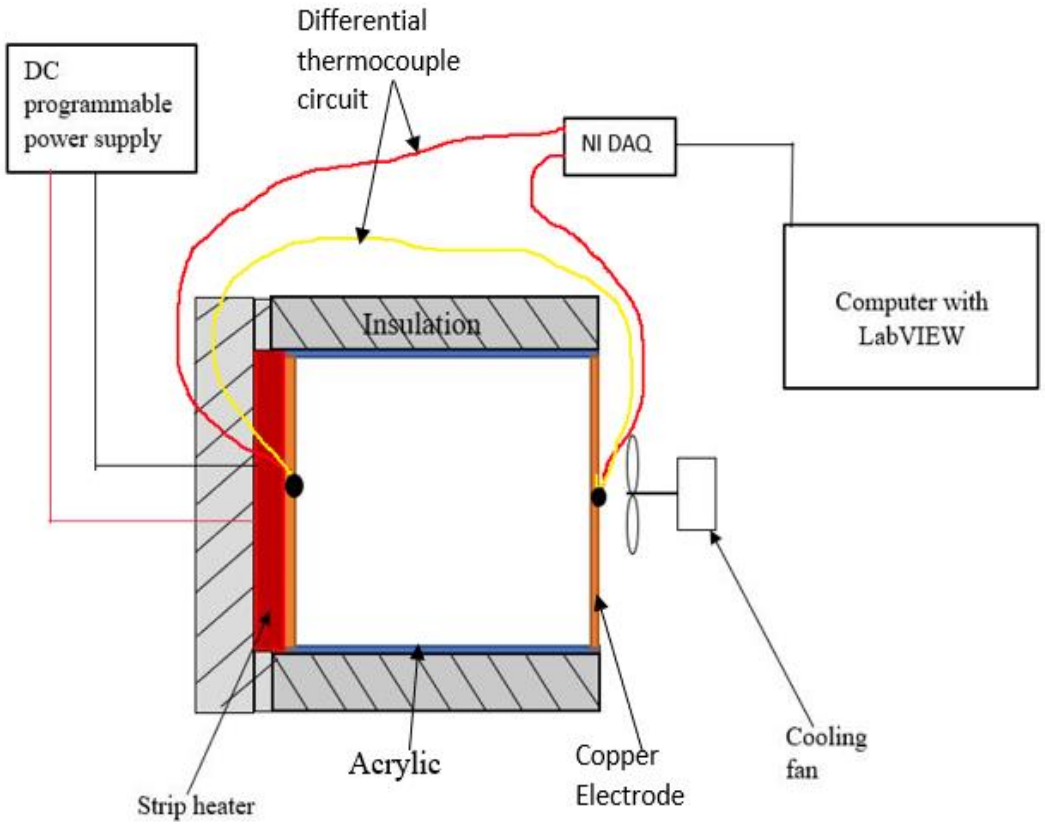

Figure 4.1. Schematic Diagram of the Experimental Setup

The remaining end of the thermocouple is inserted into the NI-9213 thermocouple module coupled with an NI cDAQ-9171 chassis connected to the computer through USB to take data via LabVIEW. Afterwards, the heating element (strip heater) is attached to the copper electrode using Silicone Heat Sink Compound and then connected to the power supply – two Protek P6000 and a BK Precision programmable DC power supply connected in series. All but the cooling side of the brick is insulated with 5.6-*mm*-thick ASTM C 612 mineral fiber block and board thermal insulation, held firmly with tape (see figure 4.2). A 12-*V*

brushless DC cooling fan is attached to the cold side of the copper plate and connected to a 12-*V* DC power supply. With the USB connected to the laptop, the LabVIEW code is configured to record the potential difference instead of temperature, and later translated into temperature using the polynomial function determined previously.

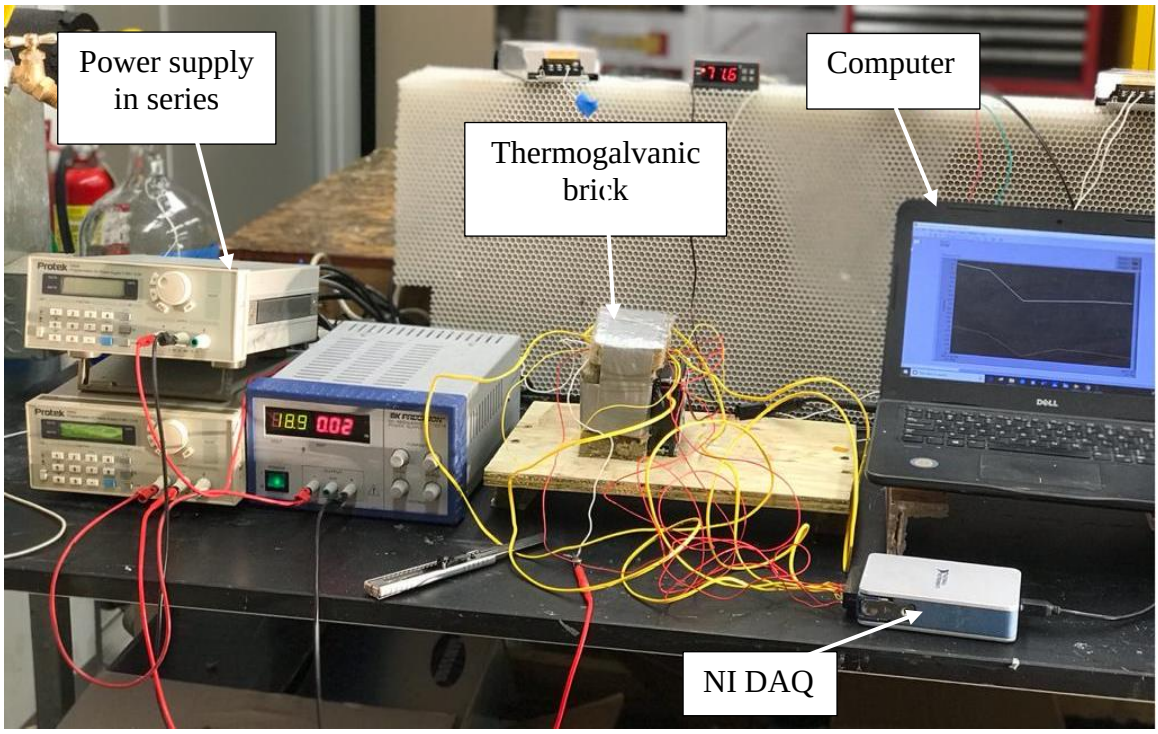

Figure 4.2. An image of the Experimental Setup

4.3. Experimental Procedure with Electrolyte in the Thermogalvanic Brick

The TPMS lattice structure for each experiment is placed in the acrylic box sandwiched between the copper electrodes. The chamber is filled entirely with electrolyte and covered. The brick is properly insulated to reduce heat losses. The cooling fan and power supplies are turned on, but before that, we make sure the connection is right to avoid explosion since

they are connected in series. Data are recorded using LabVIEW with a sampling rate set to 1 *Hz* and a time delay of 500 milliseconds. The system takes about 20 to 30 minutes to reach steady state. For each experiment, a new electrolyte is used but before that, the copper electrodes are first cleaned with isopropyl alcohol and sanded first with 220 grit sandpaper and polished with 600 grit sandpaper, to eliminate oxidation or residue of the electrolyte on the electrode.

4.1. Uncertainty Analysis

Considering a general case in which the experimental result, *f*, is a function of *J* variables x_i, the uncertainty in these results can be expressed as

$$U_f = \sqrt{\left(\frac{\partial f}{\partial x_1}U_{x_1}\right)^2 + \left(\frac{\partial f}{\partial x_2}U_{x_2}\right)^2 + \left(\frac{\partial f}{\partial x_3}U_{x_3}\right)^2 + \ldots + \left(\frac{\partial f}{\partial x_J}U_{x_J}\right)^2}, \tag{4.1}$$

where U_f is the uncertainty of the calculated variable $f(x_1, x_2, x_3 \ldots)$ and $U_{x_1}, U_{x_2}, U_{x_3}, \ldots$ the uncertainty in the measured variables x_i [35] .

Taking, for instance, the uncertainty of power input, it can be evaluated using

$$U_W = \sqrt{\left\{\left(\frac{\bar{V}_2}{R}U_{V_1}\right)^2 - \left(\frac{\bar{V}_1\,\bar{V}_2}{R}U_R\right)^2 + \left(\frac{\bar{V}_1}{R}U_{V_2}\right)^2\right\}}. \tag{4.2}$$

Table 4.1 and 4.2 shows the measured and calculated accuracies respectively.

Table 4.1. Accuracy of Measured Variables

Measured Variable	Accuracy	Unit
Temperature	± 0.5	℃
Voltage	2	%

Table 4.2. Maximum Values of Uncertainty for Calculated Variables

Calculated Variable	Maximum uncertainty	Unit
Power input	± 5.8	%
Thermal Resistance	± 6.2	%

Chapter 5

RESULTS AND DISCUSSION

Because of the new, smaller prototype designed for the current experiments, we achieved our goal of significantly reducing the time required to achieve steady state, from 3 – 4 hours (in previous experiments) to 25 – 30 minutes, as shown in figure 5.1. It shows a steady rise in ΔT, and between 20 to 30 *min* the temperature becomes steady.

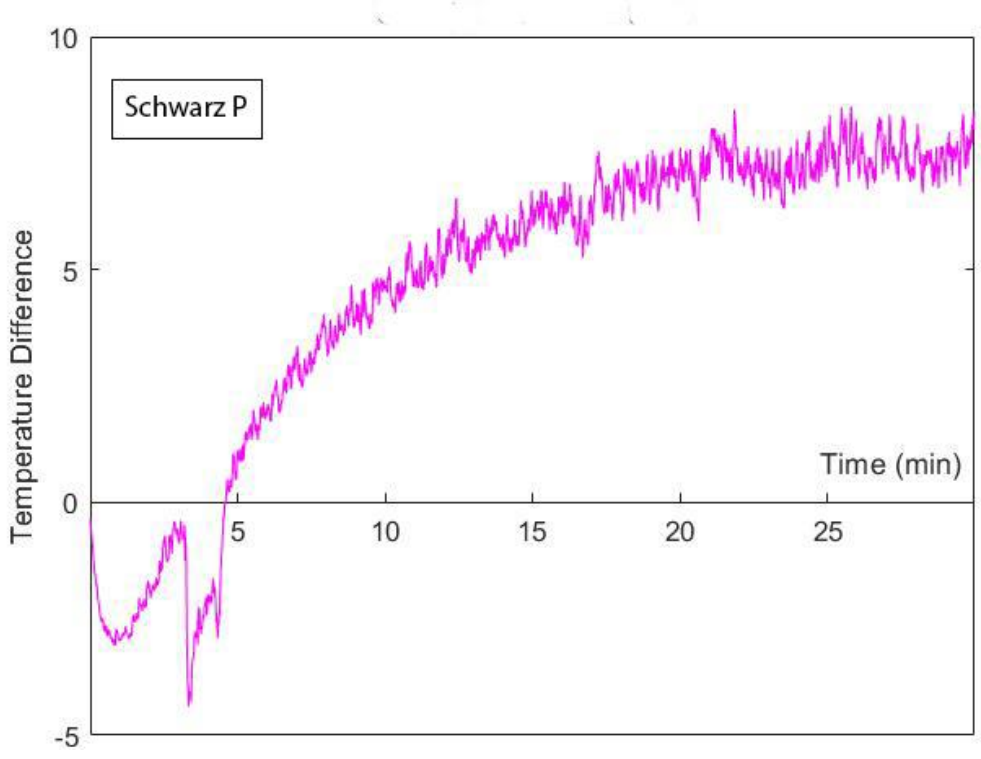

Figure 5.1. Temperature Profile of Schwarz P Showing a Steady Rise Before Steady State for an Experiment with Electrolyte in the Thermogalvanic Brick.

Table 5.1 gives a summary of the properties of the TPMS structures used for all the experiments conducted.

Table 5.1. Geometric Properties of the TPMS Structures used for all Experiments.

	No. of Unit Cell	Volume Fraction	Cross-sectional area including voids (m^2)
TPMS Structures	8	0.3	1.6×10^{-3}

5.1. Cross Sectional Area and Surface Area to Volume Ratio

The surface area and volume of the TPMS models were measured using Autodesk Netfabb and their ratios were calculated as tabulated in table 5.2. In order to evaluate the actual volume of these models after printing, we measured them experimentally. Here, each of the structures were immersed in a beaker of a known volume of water. The volume of water displaced was measured by subtracting the initial volume from the final volume of water after immersion. The results are also shown in table 5.2. As can be seen in Table 5.2, Split P has the largest cross-sectional area of all the TPMS, hence, heat is better distributed. The volumes obtained experimentally are slightly higher than measured in Netfabb, especially IWP model. This is as results of Photopolymer resin trapped in its hollow cell space when 3D printing the structure. Split P has the highest Surface area/volume ratio amongst the TPMS structures.

Table 5.2. Surface Area to Volume Ratio of the Developed TPMS Models Obtained Experimentally and from Netfabb.

Model	Surface Area (cm^2)	Volume (Netfabb) (cm^3)	Volume (experimentally) (cm^3)	Surface Area/Volume (Netfabb) (cm^{-1})	Surface Area/Volume (experimentally) (cm^{-1})
Split P	342.273	18.905	24	18.1049	14.2613
IWP	209.811	19.002	28	11.0415	7.4933
Schwarz P	166.477	19.008	21	8.7610	7.9275
Gyroid	214.738	18.958	23	11.327	9.3364

5.1.1. Volume Fraction

Although the volume fraction for all the model is the same, it turns out to be different after 3D printing. Ideally, the volume fraction should be 0.3 for all the structures but from Table 5.3, we can see the deviation. The total volume of the TPMS structures is 64 cm^3.

Table 5.3. Volume Fraction of Each TPMS Structure Determined Experimentally.

Models	Volume (cm^3)	Volume fraction
Split P	24	0.375
Schwarz P	21	0.3281
IWP	28	0.4375
Gyroid	23	0.3594

5.2. Experimental Results

A number of experiments with and without electrolytes in the thermogalvanic brick were performed as outlined in the procedure section. With the reasons stated in Chapter 3.1, experiments on Split P, IWP, Gyroid, and Schwarz D were conducted with electrolyte in the thermogalvanic brick. To validate our findings, two more sets of experiments were performed under the same conditions. The results from the experimental tests without electrolyte (air) were compared to the numerical predictions in a previous MS thesis [36].

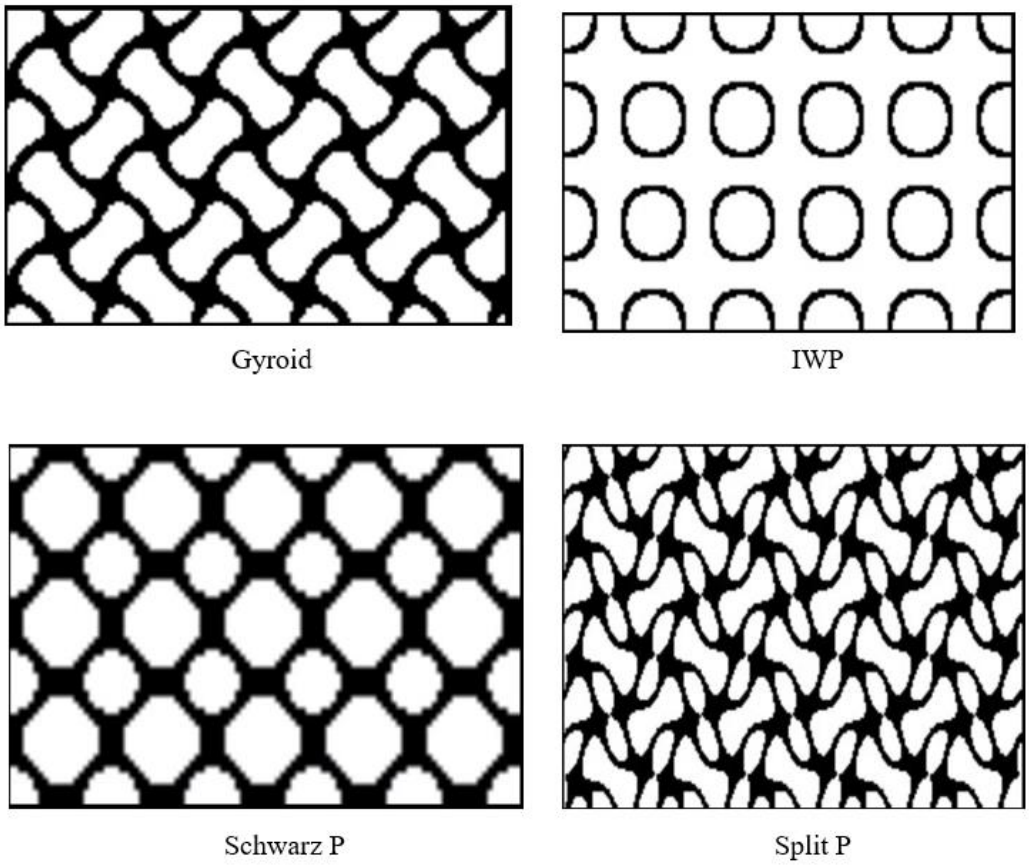

Figure 5.2. An Image of the Cross-Sectional View and Geometrical Patterns of a Unit Cell in Each TPMS Structure [9]. The White Represents Void Spaces and the Black is the Solid Material in the Structures

5.2.1. Experimental Results for TPMS Structures with Electrolyte in the Thermogalvanic Brick

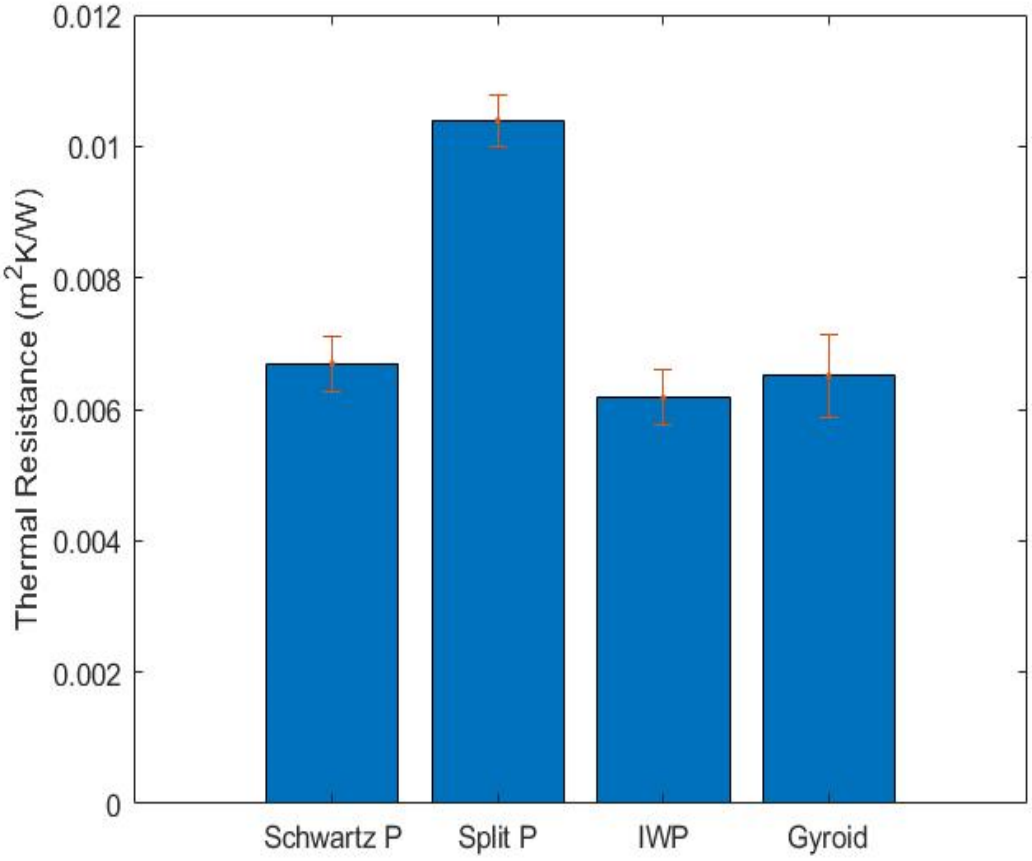

Figure 5.3. Results from the First Set of Experiments of Thermal Resistances of the Various TPMS Lattice Structures with Electrolyte.

A higher temperature gradient gives a high thermal resistance. Here, Split P shows the highest in thermal resistance with the rest hovering around the same values at a margin of 0.001 m^2KW^{-1}. For this set of experiment, IWP performed least with temperature gradient and, ultimately, thermal resistance. The geometry of the TPMS structures; the surface area/volume ratio, cell alignment, volume fraction, patterns of the cells, etc., plays a major

role in these variations. Although the number of unit cells and volume fraction are the same for all structures, the surface area/volume ratios, variations in the cell alignment; thus, parallel to heat flow, and the geometrical patterns as shown in figure 5.2, explains the differences in temperature gradients and ultimately the thermal resistances. From Table 5.2, Split P shows a higher surface area/volume ratio, therefore, heat is distributed properly. Also, from figure 5.2, it can be seen that Split P has the least void space with a complex geometrical pattern (see figure 1.8). The rate of heat flow in this case is lesser compared to the rest, ensuring high temperature gradient and therefore, higher thermal resistance.

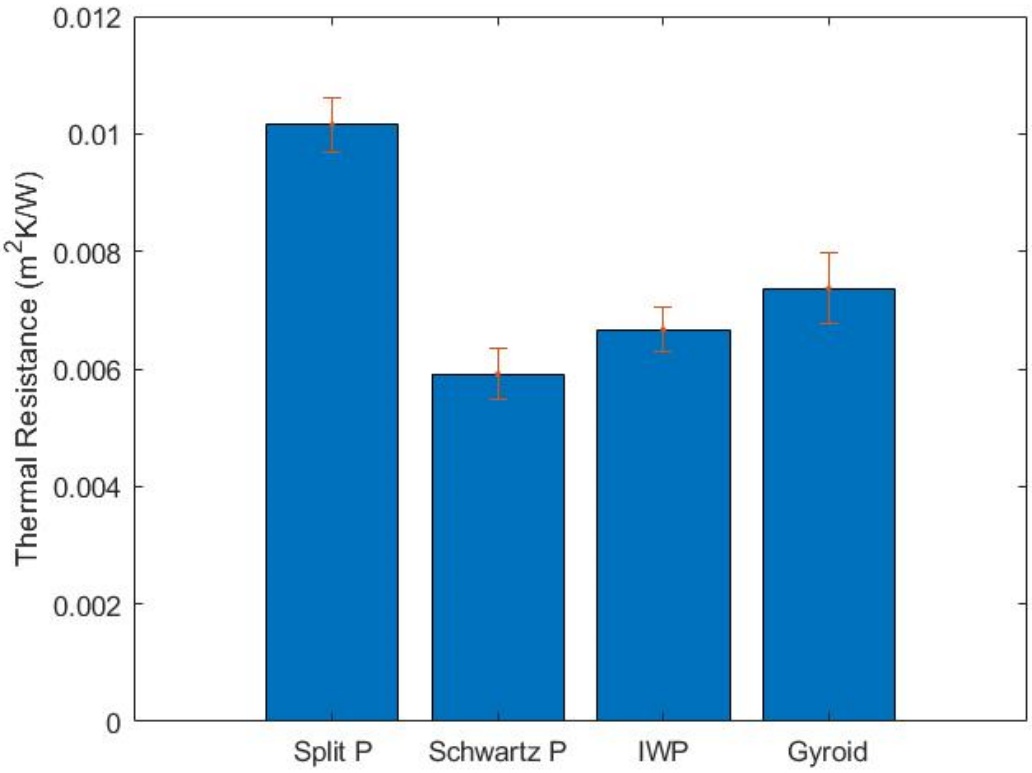

Figure 5.4. Thermal Resistances of the Different TPMS Structures for the Second Set of Experiments, also with Electrolyte.

The results are pretty consistent for the second set of experiment. Split P again shows highest in thermal resistance.

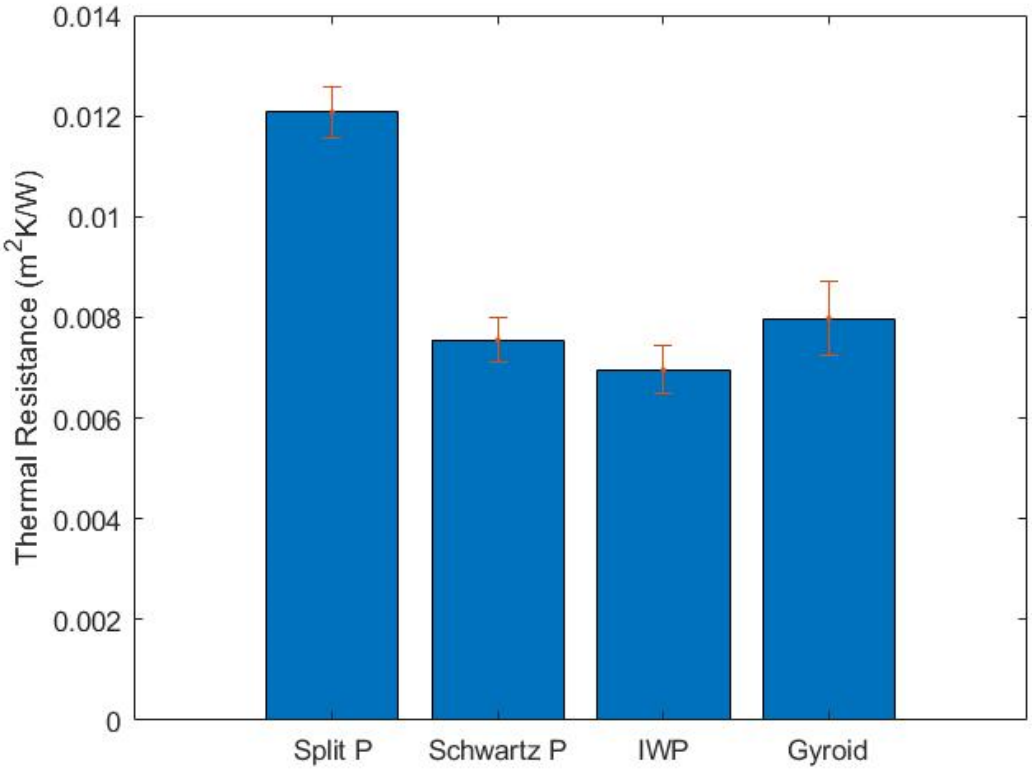

Figure 5.5. Thermal Resistances of the Different TPMS Structures for the Third Set of Experiments, also with Electrolyte.

From the results of all three sets of experiments (figures 5.3, 5.4 and 5.5), Split P consistently gave the highest temperature gradient and hence, thermal resistance. Although the results for the rest of the structures show some discrepancies, IWP conveys the least thermal resistance followed by Schwarz P. IWP and Schwarz P have lower surface area/volume ratio, moreover, their geometries are such that (figures 1.8 and 1.9) the cells are aligned horizontally, and thus parallel to the flow of heat with bigger void spaces (figure

5.2). These characteristics guarantee high heat flux across the cell (from the hot to the cold copper electrode), consequently reducing the temperature gradient as it provides relatively less resistance to heat compared to Split P. Of all four structures, Split P has the smallest size void spaces in the cell with the highest surface area/volume ratio. These properties inhibit the rate of heat flow to the cold copper plate, resulting in a high-temperature gradient. The highest mean temperature recorded for the experiments with electrolyte was 14.23℃ for the Split P case.

5.3. Comparing Experimental Results to Previous MS Thesis Numerical Predictions [36].

In a previous work [36], the thermal resistances of only Gyroid and Schwarz D TPMS structures in air were evaluated, hence in comparing my experimental results, I took into consideration just these two TPMS lattice structures. Thermal analysis was performed on these structures for different numbers of unit cells and cross-sectional area, however, the closest to my results is the one with 10unit cells. Here, experiments were conducted without electrolyte (air) in the thermogalvanic brick. This is to ensure the same conditions as stated in the previous thesis work [36]. As shown in figure 5.7, thermal pads were attached to the TPMS structure before placing it in the thermogalvanic brick case to make sure there is good thermal contact with the copper electrode. This was done to alleviate the discrepancies in temperature measurement that will arise due to the gap between the electrode and the structure.

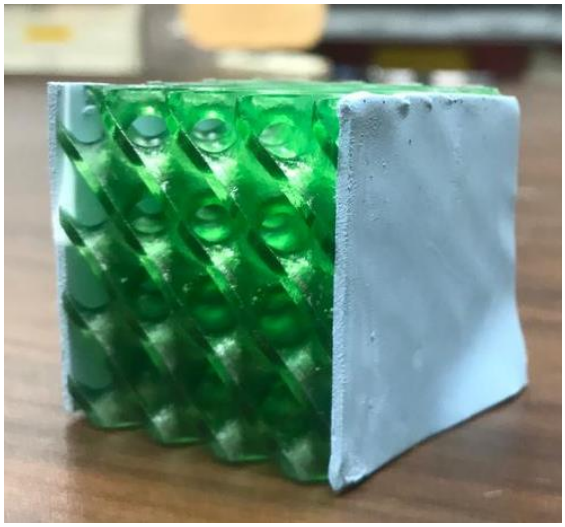

Figure 5.6. An image of the Schwarz D TPMS Structure with a Thermal Pad on Opposite Sides.

Table 5.4. Comparison of the Thermal Resistance of Schwarz D and Gyroid Results Simulated in a Previous Thesis [36] with Current Measured Values for a Heat Flux Of 1053.9 $W\,M^{-2}$. The Light Green Shade Indicates the Current Experimental Results.

	Gyroid		Schwarz D	
	Previous work (simulation)	My results (measured)	Previous work (simulation)	My results (measured)
No. of Unit cell	10	8	10	8
ΔT (K)	25	118.4	25	108.5
Cross-sectional area (m^2)	2.4785×10^{-3}	1.6×10^{-3}	1.8302×10^{-3}	1.6×10^{-3}
Heat Flux (W/m^2)	66.473	1053.9	67.03	1053.9
R_{th} (m^2K/W)	0.3769	0.1538	0.373	0.1408

From table 5.2, the thermal resistances from my experimental results are less than half what was recorded in the previous study. Although we recorded a very high temperature difference, which is one of the primary factors affecting the thermal resistances, it did not

suffice for the thermal resistance because of the difference in other factors such as the heat flux and the number of unit cells, among others. The heat fluxes utilized in the preceding work are much lower.

Another set of experiments was performed with a reduced heat flux. Technically, the thermal resistance is independent of the heat flux but there was an increase in the thermal resistance; however, they are still low compared to the results in the prior work (table 5.3).

Table 5.5. A Chart Comparing the Thermal Resistance of Schwarz D and Gyroid Results from Previous Thesis Report [36] with Mine for a Heat Flux of 328.23 Wm^{-2}. The Light Green Shade is the Result of my Experiments.

	Gyroid		Schwarz D	
	Faisal's	My results	Faisal's	My results
No. of Unit cell	10	8	10	8
ΔT (K)	25	59.7	25	52.7
Cross-sectional area (m^2)	2.4785×10^{-3}	1.6×10^{-3}	1.8302×10^{-3}	1.6×10^{-3}
Heat Flux(W/m^2)	66.473	328.23	67.03	328.23
R_{th} (m^2K/W)	0.3769	0.182	0.373	0.16

5.4. Account for Heat Loss to the Ambient

Of paramount importance to our discussion is to accurately calculate the amount of heat lost to the ambient. This is what helps to justify the assumption that the rate of heat flow is one-dimensional. The heat was lost to the ambient through conduction, convection, and radiation. The effect of heat loss through radiation was only significant for the case of the experiment run with just air in place of electrolyte (as shown in table 5.5). This is because higher temperatures (between 100℃ – 160℃) were recorded.

Table 5.6. Summary of the Percentage Heat Loss to the Ambient for each Set of Experiments with or without Electrolyte

Type of experiment	Total power input (W/m^2)	Net power (W/m^2)	Power loss (W/m^2)	Percentage (%)
with electrolyte	1282.175	1053.904	228.271	17.8
without electrolyte	1282.175	695.003	587.172	45.8
	526.55	328.23	198.32	37.7

From table 5.4, the rate of heat loss is pretty high, especially for the experiment without electrolyte in the thermogalvanic brick. Of all the losses encountered, the contribution of the different heat transfer means are summarized in table 5.5. It is seen that heat loss by radiation is negligible for the case of the experiment with electrolyte and also at a reduced heat flux in air due to the relatively lower temperatures.

Table 5.7. Percentage Contribution of the Different Heat Transfer Modes (Conduction, Convection, and Radiation)

Type of experiment	Conduction	Convection	Radiation
With electrolyte (*1282.175 Wm^{-2}*)	77.94	22.06	Negligible
Without electrolyte (*1282.175 Wm^{-2}*)	54	31.4	13.62
Without electrolyte (*526.55 Wm^{-2}*)	72.8	27.22	Negligible (0.08%)

5.5. Using the Student T–Distribution to Evaluate Thermal Resistance of each TPMS Lattice Structures

Taking the three sets of experimental tests, the Student T-Distribution was used to determine the sample mean for each of the TPMS lattice structures and the boundaries each acceptable thermal resistance should fall in. The following equations was used to calculate the propagation of uncertainty taken at 95% confidence level. Table 5.6 gives the mean thermal resistances and the uncertainties for each TPMS structure.

$$Sample\ Average\ =\ \bar{X}\ =\ \sum_{1}^{n}\frac{X_i}{n} \tag{5.1}$$

$$Sample\ Standard\ Deviation\ =\ S_x\ =\ \sqrt{\frac{1}{n-1}\sum_{1}^{n}(X_i\ -\ \bar{X})^2,} \tag{5.2}$$

and

$$P_{\bar{x}} = t_{a/2,v} \frac{S_x}{\sqrt{n}} (95\%) \quad (5.3)$$

where n is the number of samples and $t_{a/2,v}$ the probability distribution function found using the T-table.

Table 5.8. Range of Thermal Resistance Uncertainties at 95% Confidence Level using T-distribution Table.

	Mean	SD	Uncertainty
Split P	0.012	0.00093	±0.0017
Schwarz P	0.0074	0.00073	±0.0013
IWP	0.0073	0.00037	±0.0007
Gyroid	0.00803	0.00065	±0.0012

After employing the Student's T-distribution table to statistically estimate the mean thermal resistance using the three sets of experiments as shown in table 5.6, the results were plotted in figure 5.7. Statistically, the thermal resistances of Schwarz P and IWP are almost the same. The thermal resistance of Split P was used in comparing the thermal resistance of a regular brick (see table 5.7).

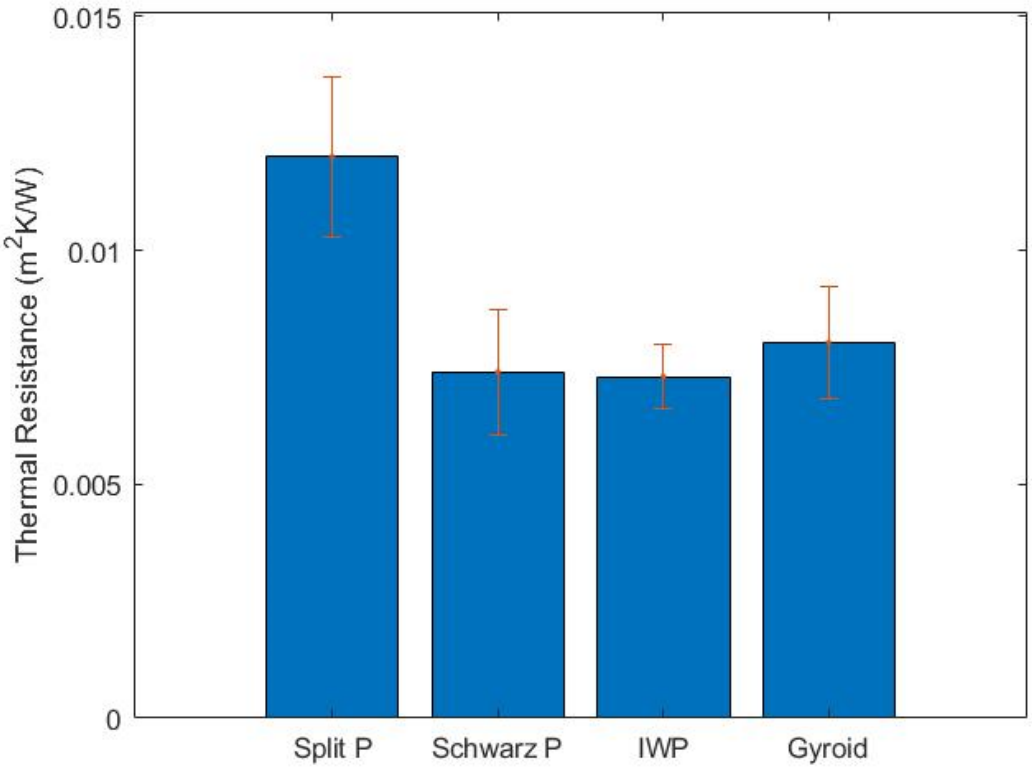

Figure 5.7. Average Thermal Resistances for all the TPMS Structures (with electrolyte) with the Error Bars Computed using the Student-T distribution.

5.6. Thermal Resistance of Split P Against a Conventional Brick

After calculating for the thermal resistance of each TPMS structure investigated (see figure 5.7), that of Split P was compared to a common conventional brick of a thermal conductivity 1.30 $Wm^{-1}K^{-1}$. The thermal resistance of the brick was calculated at the same dimensions as that of the Split P structure, thus, 40x40x40 *mm.* Table 5.6 shows the comparison in the thermal resistances.

Table 5.9. A Table Comparing the Thermal Resistance of a Conventional Brick Against the TPMS Structures

	Conventional Brick	Split P
Thermal Resistance (m^2K/W)	0.03	0.012

Considering the void spaces in the structures that allows heat transfer through the electrolyte, the thermal resistance of Split P can be considered good enough.

5.7. Thermal Conductivity of the TPMS Structures (Split P)

Taking the distribution of the electrolyte in the TPMS structure as composite material, we can calculate the upper or lower bound of the thermal conductivity knowing the thermal resistance of the composition. Now, instead of having the electrolyte evenly distributed in the structure, let suppose the TPMS structure is melted to form a solid and the electrolyte fill up the rest of the space as shown in figure 5.8. All the TPMS structures used are made up of 30% volume fraction that is why it makes up small portion of the brick. Here, we assume a series connection TPMS structure with the electrolyte.

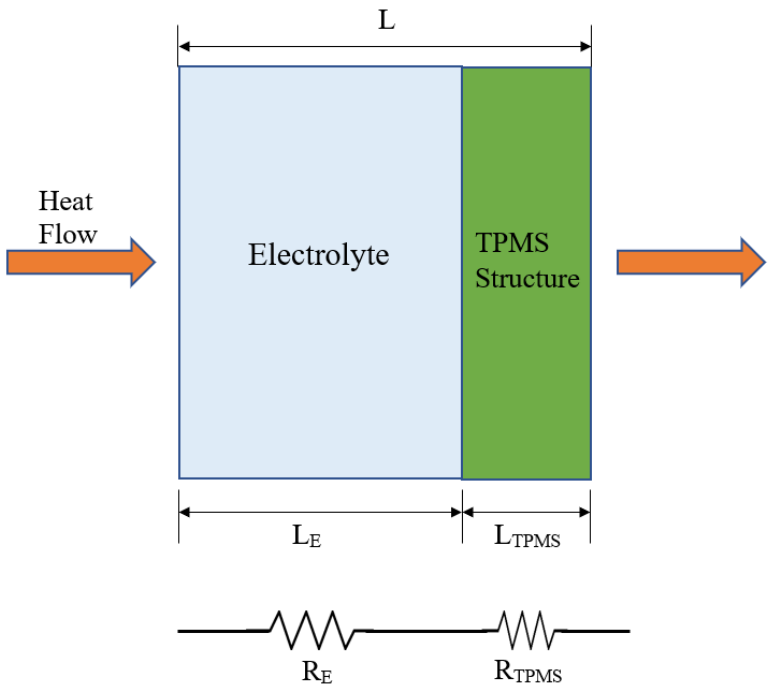

Figure 5.8. Electrolyte and TPMS Structure Arranged in Series Connection.

The total thermal resistance, R_{TOTAL} is given by the sum of the thermal resistances of the structure, R_{TPMS} and that of the electrolyte, R_E .

$$R_{TOTAL} = R_E + R_{TPMS} = \frac{L_E}{K_E A_E} + \frac{L_{TPMS}}{K_{TPMS} A_{TPMS}}, \tag{5.4}$$

where L_E the length of the electrolyte, L_{TPMS} the length of the TPMS structure, K_E the thermal conductivity of electrolyte, K_{TPMS} the thermal conductivity of the TPMS structure, A_E and A_{TPMS} are the cross-sectional area of the electrolyte and the TPMS structures respectively.

The volume fraction of the TPMS structure, φ can be expressed as;

$$\varphi = \frac{A\,L_{TPMS}}{A\,L} = \frac{L_{TPMS}}{L}, \tag{5.5}$$

where A, the cross-sectional area of the brick and L, the total length. Hence, we can rewrite equation 5.1 as

$$R_{TOTAL} = \frac{(1 - L_{TPMS})\,K_{TPMS}\,A + L_{TPMS}K_E A}{K_{TPMS}\,K_E A^2}. \tag{5.6}$$

After several simplification, the total thermal resistance becomes;

$$R_{TOTAL} = \frac{L[(1 - \varphi)\,K_{TPMS} + \varphi K_E]}{K_{TPMS}\,K_E A}. \tag{5.7}$$

Assuming the electrolyte is water with thermal conductivity of 0.6 $Wm^{-1}K^{-1}$ at 25°C, the thermal conductivity of the TPMS structure (Split P) was calculated as 0.346 $Wm^{-1}K^{-1}$.

Chapter 6

CONCLUSION

For a fact, incorporating TPMS lattice structures in thermogalvanic bricks improves the thermal resistance; however, the extent varies from one structure to another. Interestingly, with a net heat flux of 1053.39 W/m^2 for the different sets of experiments conducted with electrolyte, Split P consistently gave a relatively higher temperature difference and, therefore, higher thermal resistances ($12.1x10^{-3}$ $m^{-2}K/W$) followed by Gyroid. IWP proved the least in thermal resistances, although there are discrepancies in the consistencies for the different sets of experiment testing. The main reason for a higher thermal resistance in Split P depends greatly on its higher surface area/volume ratio (see table 5.2) and the complex architectural nature (see figure 1.9), as explained in chapter 5. In the previous study on these structures [9], the mechanical properties were investigated for just the Schwarz D, Schwarz P, and Gyroid TPMS structures, and led to the conclusion that Gyroid and Schwarz D will be a good fit for thermogalvanic brick applications. Nevertheless, with the thermal properties of Split P, it will be useful to also consider it for this application.

Properly estimating the rate of heat losses has a major effect on the thermal resistances because errors propagate into these results. Out of the 1282.175 Wm^{-2} power supplied to the heater for the tests with just air, only about 64% actually went through the system. The rest is lost to the ambient; therefore, proper insulation will be required to also reduce the losses. These losses are especially higher in the experiment without electrolyte in the thermogalvanic brick because of higher temperatures – as high as 160°C.

The effect of the differential thermocouple configuration is seen in the uncertainty of the thermal resistance. The coefficient ($\sqrt{2}$) of the measured temperature errors is eliminated therefore reducing the promulgating uncertainty associated with the thermal resistance results.

6.1. Effect of SLA and FDM 3D Printing Method on the Thermal Resistance of the TPMS Structures.

The effect of 3D printing method on thermal properties of a material is usually paramount for composite materials such as Metal/Polymer [37] [38] [39] and organic/polymer [40]. Most research have been focused on investigating the effect of a 3D printing method on the mechanical properties of a material. Effect on the thermal properties are usually elucidated for composite material. However, in both SLA and FDM 3D printing, assuming a same material type, the choice of printing process parameters can affect the mechanical properties of the structure and consequently, the thermal properties. The main difference between the two is the way layers are deposited.

For FDM printing, parts are usually not printed solid in order to reduce the print time and save material. Instead, the outer perimeter (shell) is traced and the interior is filled with an internal, low-density structure, called the infill. In most FDM 3D printers used, the default setting infill density is 25% and 1mm shell thickness [41]. These parameters have great influence on the end product. Moreover, since the molten material is pressed against the previous layer, it shape is deformed to an oval. This means that FDM parts will always have a wavy surface, even for low layer height, and that small features, such as small holes or thread may need to be post processed after printing as shown in figure 6.1.

Figure 6.1. The Layer Lines of an FDM. these are Usually Visible [41].

Not choosing the optimal parameters such as the percentage infill, shell thickness, print orientation, extruder temperature, etc. for a structure, can affect influence thermal properties, i.e. thermal resistance. The void created inside the structure because of the choice of infill density and the layer thickness will ensure small pores in the structure reducing it robustness. Heat will be absorbed due to the surface roughness and therefore, affecting the thermal resistance of the structure.

Also, based on the complexity of the TPMS structures, the type of FDM 3D printer used has an influence on the thermal properties. There is a need for support material in printing these structures, however, they cannot be easily removed when a single extruder FDM 3D printer is utilized. In a dual extruder 3D printer, a soluble material is used as a

support material, therefore, can be dissolved in an acid/base bath. The support material will increase the surface area of the structures, hence, affecting heat flux and thus, thermal resistance.

In SLA 3D printing, a post UV-curing is needed to further enhance the physical properties of the structure since the photo resins are not fully crosslinked after the 3D printing. Printing parameters such as printing orientation [42] [43] and layer thickness [44], exposure time, usually influence the mechanical properties of the structures. To enhance the thermal properties, nanofillers are introduced to the photopolymer matrix [45]. Here, support material can be easily removed so it does not affect the surface area as in the case of FDM printing.

Ultimately, either SLA or FDM can influence the thermal resistance of the TPMS structures. The extend of the effect depends on the choice of the printing process parameters. However, it is minimal in the SLA 3D printing process.

Chapter 7

FUTURE WORK AND RECOMMENDATION

The primary focus of this project is to increase the power output of the thermogalvanic brick. For this thesis, only the thermal resistances of the structures were estimated. However, to increase thermal resistance and the temperature gradient without jeopardizing the rate of ionic transfer in the system, it is recommended to consider insertion of a membrane in the structures. Inserting a correct membrane material and optimizing the position in the structures will allow ionic transport yet be highly thermally resistive to maintain a large temperature gradient between the electrodes. This act will reduce the intrinsic internal resistance and thereby increase the power output of the thermogalvanic brick [46]. From equation 7.1, it is evident that the power efficiency, η, given by

$$\eta = \frac{\alpha^2 R_{th} \Delta T}{4 R_{int}} \tag{7.1}$$

where α is Seebeck coefficient, R_{th} the thermal resistance, R_{int} the ionic resistance and ΔT the temperature difference. Clearly, the thermogalvanic brick will benefit by maximizing the ratio R_{th}/R_{int}, that is, maximizing ionic transport while minimizing thermal transport.

Secondly, the electrolyte used only allows reduction of copper ions in one direction. For the practical application of thermogalvanic bricks, we need an electrolyte that reacts reversibly. Therefore, going forward iron (II/III) perchlorate will be a good option which is proven to perform better than $[Fe(CN)_6]^{3-}/[Fe(CN)]^{4-}$ [47].

Also, it is good investigate the performance of hollow bricks as thermogalvanic bricks, that is, we replace the TPMS structures with a hollow brick to see their performance.

REFERENCES

[1] L. Livermore, "Estimated U.S. Energy Consumption in 2017: 97.7 Quads," in *National Laboratory*, 2017.

[2] Linke, M. Stijepovic and P., "Optimal Waste Heat Recovery and Reuse in Industrial Zones," *Energy*, vol. 36, pp. 4019 - 4031, 2011.

[3] Cheng-Ting Hsu, Da-Jeng Yao, Ke-Jyun Ye, and Ben Yu, "Renewable energy of waste heat recovery system for automobiles," *Journal of Renewable and Sustainable Energy*, vol. 2, p. 013105, 2010.

[4] I. Dincer, "On Thermal Energy Storage Systems and Applications in Buildings," *Energy and Buildings*, vol. 34, pp. 377 - 388, 2002.

[5] I. E. Agency, "World Energy Outlook," *International Energy Agency*, 2019.

[6] ChunzeYan, Liang Hao, Ahmed Hussein, Philippe Young, "Ti–6Al–4V triply periodic minimal surface structures for bone implants fabricated via selective laser melting," *Journal of the Mechanical Behavior of Biomedical Materials*, vol. 51, pp. 61-73, 2015.

[7] I. Maskery, A. Hussey, A. Panesar, A. Aremu, C. Tuck, I. Ashcroft, R. Hague, "Insights into the mechanical properties of several triply periodic minimal surface lattice structures made by polymer additive manufacturing," *Polymer*, vol. 152, pp. 62 - 71, 2018.

[8] Ian Maskery, Alexandra Hussey,Ajit Panesar, Adedeji Aremu,Christopher Tuck, Ian Ashcroft andRichard Hague, "An investigation into reinforced and functionally graded lattice structures," *Cellular Plastics*, vol. 53, pp. 151-165, 2016.

[9] B. Obeng, "Effect of Triply Periodic Minimal Surface Structures on Mechanical and Power Conversion Performance of Thermogalvanic brick," Tempe, 2019.

[10] Mua, T. I. Quickenden and Y., "A Review of Power Generation in Aqueous Thermogalvanic Cells," *The Electrochemical Society*, 1995.

[11] E. Bouty, "Phénomènes Thermo-électriques et Électro-thermiques au Contact d'un Métal et d'un Liquid [Thermo-electric and Electro-thermal Phenomena at the

Contact between a Metal and a Liquid," *Journal de Physique [Journal of Physics,* vol. 9, pp. 229 - 241, 1880.

[12] Andrey Gunawan, Hechao Li, Chao-Han Lin, Daniel A. Buttry, Vladimiro Mujica, Robert A. Taylor,Ravi S. Prasher, Patrick E. Phelan, "The amplifying effect of natural convection on power generation of thermogalvanic cells," *International Journal of Heat and Mass Transfer,* p. 15, 2014.

[13] Herman A. Liebhafsky, Schenectady, N.Y., "THERMOGALVANIC CELL," *General Electric Company, a corporation of New York,* p. 5, 1959.

[14] A. Gunawan, "Electrolyte- and Transport-Enhanced Thermogalvanic Energy Conversion," ARIZONA STATE UNIVERSITY, Tempe, 2015.

[15] Andrey Gunawan , Chao-Han Lin , Daniel A. Buttry , Vladimiro Mujica , Robert A. Taylor , Ravi S. Prasher & Patrick E. Phelan, "Liquid Thermoelectrics: Review of Recent And Limited New Data of Thermogalvanic Cell Experiments," *Nanoscale and Microscale Thermophysical Engineering,* vol. 4, pp. 304-323, 2013.

[16] Holeschovsky, Ulrich Bernd, "Analysis of Flooded Flow Fuel Cells and Thermogalvanic generators," *Thesis,* 1994.

[17] Seok Woo Lee, Yuan Yang, Hyun-Wook Lee, Hadi Ghasemi, Daniel Kraemer, Gang Chen & Yi Cui, "An electrochemical system for efficiently harvesting low-grade heat energy," *Nature Communications,* no. 2013, 2014.

[18] Hualong Ma, Xiaochen Wang, Yanqiu Peng, Hanqing Peng, Meixue Hu, Li Xiao, Gongwei Wang, Juntao Lu, and Lin Zhuang, "Powerful Thermogalvanic Cells Based on a Reversible Hydrogen Electrode and GasContaining Electrolytes," *ACS Energy Letters,* vol. 4, pp. 1810-1815, 2019.

[19] Eric A. Lord, and Alan L. Mackay, "Periodic minimal surfaces of cubic symmetry," *Research Articles,* pp. 346-362, 2003.

[20] A. H. Schoen, "Infinite periodic minimal surface without self-intersection," *NASA TN D-5541,* 1970.

[21] P. J. a. J. K. Gandy, "Exact computation of the triply periodic g (gyroid') minimal surface," *Chemical Physics Letters ,* vol. 321, pp. 363-371, 2000.

[22] Ajit Panesar, Meisam Abdi, Duncan Hickman, Ian Ashcroft, "Strategies for functionanlly graded lattice structures derived using topology for Additive Manufacturing," *Addittive Manufacturing*, vol. 19, pp. 81-94, 2018.

[23] D. Yoo, "New paradigms in internal architecture design and freeform fabrication of tissue engineering porous scaffolds," *Medical Engineering & Physics*, pp. 762-776, 2012.

[24] Anna Aimar, Augusto Palermo, and Bernardo Innocenti, "The role of 3D printing in Medical Applications: A state of the Art," *Journal of Healthcare Engineering*, vol. 2019, p. 10, 2019.

[25] Alexander Paolini, Stefan Kollmannsberger, Ernst Rank, "Additive manufacturing in construstion: A review on process, applications, and digital planning methods," *Additive manufacturing*, vol. 30, p. 100894, 2019.

[26] Z. Cohen, "Applications of Additive Manufacturing in Automotive Electronics: 3 Key Innovations," Nao Dimension, 03 April 2019. [Online]. Available: https://www.nano-di.com/blog/2019-applications-of-additive-manufacturing-in-automotive-electronics-3-key-innovations.

[27] Paulo Jorge Bártolo, Ian Gibson, "History of Stereolithographic Process," *Springer*, pp. 37-56, 2011.

[28] Jin, Ali Bagheri and Jianyong, "Photopolymerization in 3D Printing," *ACS Applied polymer materials*, vol. 2019, no. 4, pp. 593-611, 2019.

[29] Wikipedia, "Photopolymer," 04 March 2020. [Online]. Available: https://en.wikipedia.org/w/index.php?title=Photopolymer&oldid=943807168.. [Accessed 10 April 2020].

[30] Kudo3D, "SLA 3D Printing: Difference in Laser and DLP Light Pattern Generation," Kudo3D, [Online]. Available: https://www.kudo3d.com/sla-3d-printing-difference-in-laser-and-dlp-light-generation/. [Accessed 10 April 2020].

[31] Chao-Han Lin, Andrey Gunawan , Patrick E. Phelan , Daniel A. Buttry , Vladimiro Mujica , Robert A. Taylor , Ravi Prasher, "Optimization of Cell Configuration for Maximizing Performance of a Cu/Cu2+ Aqueous Thermogalvanic Cell," *ASME International Mechanical Engineering Congress and Exposition*, pp. 541-547, 2013.

[32] W. Lee, "Experimental Measurements of the Power Output of a Cu/Cu2+ Thermogalvanic Brick," *Arizona State University, Master Thesis*, p. 99, 2018.

[33] SyedWaqar Hasan1, Suhana Mohd Said1, Mohd Faizul Mohd Sabri2, Ahmad ShuhaimiAbu Bakar3, Nur Awanis Hashim4, Megat Muhammad Ikhsan Megat Hasnan1, Jennifer M. Pringle5 &Douglas R. MacFarlane, "High Thermal Gradient in Thermoelectrochemical Cells by Insertion of a Poly(Vinylidene Fluoride) Membrane," Scientific Reports, 2016.

[34] William M. Pitts, I Emil Braun, Richard D. Peacock, Henri E. Mitler, Erik L. Johnsson, Paul A. Reneke, and Linda G. Blevins, "Temperature Uncertainties for Bare-Bead and Aspirated Thermocouple Measurements in Fire Environments," *ASTM International,* 2002.

[35] Hugh WW. Coleman, W. Glenn Steele, JR, Experimentation and uncertainty analysis for engineers, Toronto: John Wiley & Sons, Inc, 1989.

[36] F. Raja, "Evaluation of Properties of Triply Periodic Minimal Surface Structures Using ANSYS," *Arizona State University,* 2019.

[37] Seyeon Hwang, Edgar I. Reyes, Kyoung-Sik Moon, Raymond C. Rumpf, and Nam Soo Kim, "Thermo-mechanical Characterization of Metal/Polymer Composite Filaments and Printing Parameter Study for Fused Deposition Modeling in the 3D Printing Process," *The Minerals, Metals & Materials Society,* vol. 44, no. 3, 2015.

[38] Suhail Mubarak, Duraisami Dhamodharan, Nidhin Divakaran, Manoj B. Kale, T. Senthil, Lixin Wu, and Jianlei Wang, "Enhanced Mechanical and Thermal Properties of Stereolithography 3D Printed Structures by the Effects of Incorporated Controllably Annealed Anatase TiO2 Nanoparticles," *Nanomaterials,* vol. 10, 2020.

[39] Razieh Hashemi Sanatgar, ChristineCampagne, VincentNierstrasza, "Investigation of the adhesion properties of direct 3D printing of polymers and nanocomposites on textiles: Effect of FDM printing process parameters," *Applied Surface Science,* vol. 403, pp. 551-563, 2017.

[40] Zixiang Weng, Jianlei Wang, T.Senthil, and LixinWu, "Mechanical and thermal properties of ABS/montmorillonite nanocomposites for fused deposition modeling 3D printing," *Materials & Design,* vol. 102, pp. 276-283, 2016.

[41] A. B. Varotsis, "Introduction to FDM 3D printing," 3D HUBS, 2020. [Online]. Available: https://www.3dhubs.com/knowledge-base/introduction-fdm-3d-printing/#what. [Accessed 23 April 2020].

[42] Rima Janusziewicz, John R. Tumbleston, Adam L. Quintanilla, Sue J. Mecham, and Joseph M. DeSimone, "Layerless fabrication with continuous liquid interface production," *Proceedings of the National Academy of Sciences of the United States of America,* vol. 42, no. 113, pp. 11703-11708, 2016.

[43] R. Hague, S. Mansour, N. Saleh & R. Harris , "Materials analysis of stereolithography resins for use in Rapid Manufacturing," *Springer,* vol. 39, pp. 2457-2464, 2004.

[44] K. Chockalingam, N. Jawahar, K.N. Ramanathan & P.S. Banerjee , "Optimization of stereolithography process parameters for part strength using design of experiments," *Springer,* vol. 29, pp. 79-88, 2006.

[45] Sungmin Park, Anna M. Smallwood, and Chang Y. Ryu, "Mechanical and Thermal Properties of 3D-Printed Thermosets by Stereolithography," *Journal of Photopolymer Science and Technology,* vol. 32, pp. 227-232, 2019.

[46] SyedWaqar Hasan, Suhana Mohd Said, Mohd Faizul Mohd Sabri, Ahmad ShuhaimiAbu Bakar, Nur Awanis Hashim, Megat Muhammad Ikhsan Megat Hasnan, Jennifer M. Pringle &Douglas R. MacFarlane, "High Thermal Gradient in Thermoelectrochemical Cells by insertion of Poly(Vinylidence Flouride) Membrane.," Scientific Reports, 2016.

[47] Ju Hyeon Kim, Ju Hwan Lee, Ramasubba Reddy Palem, Min-Soo Suh, Hong H. Lee & Tae June Kang, "Iron (II/III) perchlorate electrolytes for electrochemically harvesting low-grade thermal energy.," *Scientific Reports,* vol. 8706, 2019.

[48] J. N. Agar, "Thermogalvanic Cells in Advances in Electrochemistry and Electrochemical Engineering," P. Delahay, Interscience Publisher, New York, 1963.

[49] B. Uhalde, "Design of an experiment to test a thermogalvanic cell and building of a prototype," *Thesis,* 2019.

[50] A. Gunawan, "Electrolyte- and Transport-Enhanced Thermogalvanic Energy Conversion," *Arizona State University, PhD dissertation,* 2015.

[51] Karunesh Kant ⇑, A. Shukla, Atul Sharma, "Heat transfer studies of building brick containing phase change," *Solar Energy,* p. 10, 201.

[52] Yunus A. Cengel, Afshin J. Ghajar, Heat and Mass transfer, New York: McGraw-Hill Education, 2015.

[53] S.M. Giannitelli, D. Accoto, M. Trombetta, A. Raine, "Current trends in the design of scaffolds for computer-aided tissue engineering," *Acta Biomaterialia,* pp. 580-594, 2013.

[54] L. Brasington, "Heating, Ventilation and Air Conditioning (HVAC) Systems, the Next Building Load to Optimize," Cleantech Group, 26 June 2019. [Online]. Available: https://www.cleantech.com/heating-ventilation-and-air-conditioning-hvac-systems-the-next-building-load-to-optimize/. [Accessed 28 March 2020].

APPENDIX A

MATLAB CODE

The MATLAB code used for calculating area of cross section of the TPMS models:

```
clc
srcFile = dir('Path to your BMP Files\*.bmp');
percentageBlack = zeros(1, length(srcFile));
sum=0;
for i = 1:length(srcFile)
    filename=strcat(''Path to your BMP Files\',
srcFile(i).name);
    I=imread(filename);
    percentageBlack (1,i)=((1-nnz(I)/numel(I)));
    sum = sum + percentageBlack(1,i);
end
sum_avg = sum/length(srcFile)
area = sum_avg*40*40
```

The MATLAB code for calculating thermal resistance of the TPMS structures

```
A = xlsread('Schwartz P_resistance.xlsx');
A = A(:,4);
q_net = 1053.9 %(W/m^2)
x6 = linspace(0,15,length(A));
for k = 1:length(A)
    R_sp = A./q_net;
end

%%

C = xlsread('IWP_03182020');
C = C(:,4);
%q_net = 3573.65 %(W/m^2)
x1 = linspace(0,15,length(C));
for k = 1:length(C)
    R_IWP = C./q_net;
end

%%
D = xlsread('Gyroid_03112020');
D = D(:,4);
%q_net = 3573.65 %(W/m^2)
x1 = linspace(0,15,length(D));
for k = 1:length(D)
    R_Gy = D./q_net;
end

%%
B = xlsread('Split-P_03142020');
B = B(:,5);
%q_net = 3573.65 %(W/m^2)
x1 = linspace(0,15,length(B));
for k = 1:length(B)
    R_Split = B./q_net;
end

x_P = mean(A)
x_S = mean(B)
x_IWP = mean(C)
x_G = mean(D)

y_P=mean(R_sp);
y_S=mean(R_Split);
```

```
y_IWP=mean(R_IWP);
y_G=mean(R_Gy);
er_P= 0.063*y_P;
er_S= 0.06*y_S;
er_IWP= 0.064*y_IWP;
er_G= 0.064*y_G;

figure
plot(x_S,y_S, '*r', x_P,y_P, 'om', x_IWP,y_IWP, '+b',
x_G,y_G, '^g')
legend('Split-P','Schwartz_P', 'IWP',
'Gyroid','Location','northwest')
hold on
x = [x_S,x_P,x_IWP,x_G];
y = [y_S,y_P,y_IWP,y_G];
%errorbar(x22,y2,err, 'o')
errorbar(x,y,err,'.')
title('Thermal Resistance vs Temperature Difference')
xlabel('Temperature Difference ({\circ}C)')
ylabel('Thermal Resistance  (m^2K/W)')
ylim([0.006 0.0125])
ax = gca;
ax.XAxisLocation = 'origin';
xlim([6 13])
ylim([0.0015 0.004])


%%

% X = categorical({'Small','Medium','Large','Extra
Large'});
% X = reordercats(X,{'Small','Medium','Large','Extra
Large'});
a = categorical({'Schwartz_P', 'Split_P','IWP','Gyroid'});
%a = reordercats({'Schwartz_P', 'Split_P','IWP','Gyroid'});
figure
y = [y_P,y_S,y_IWP,y_G];
err = [er_P,er_S,er_IWP,  er_G];
%bar(a,y)
bar(y)
ylabel('Thermal Resistance (m^2K/W)')
%xticks( 1:4 );
xticklabels({'Schwartz P', 'Split P','IWP','Gyroid'});
hold on
errorbar(y, err, '.')
```

```
ylim([0 0.013])
%ylabel('Max Power Density /\DeltaT^2 (\muW/cm^2K^2)')
```

APPENDIX B

EXTRA DATA

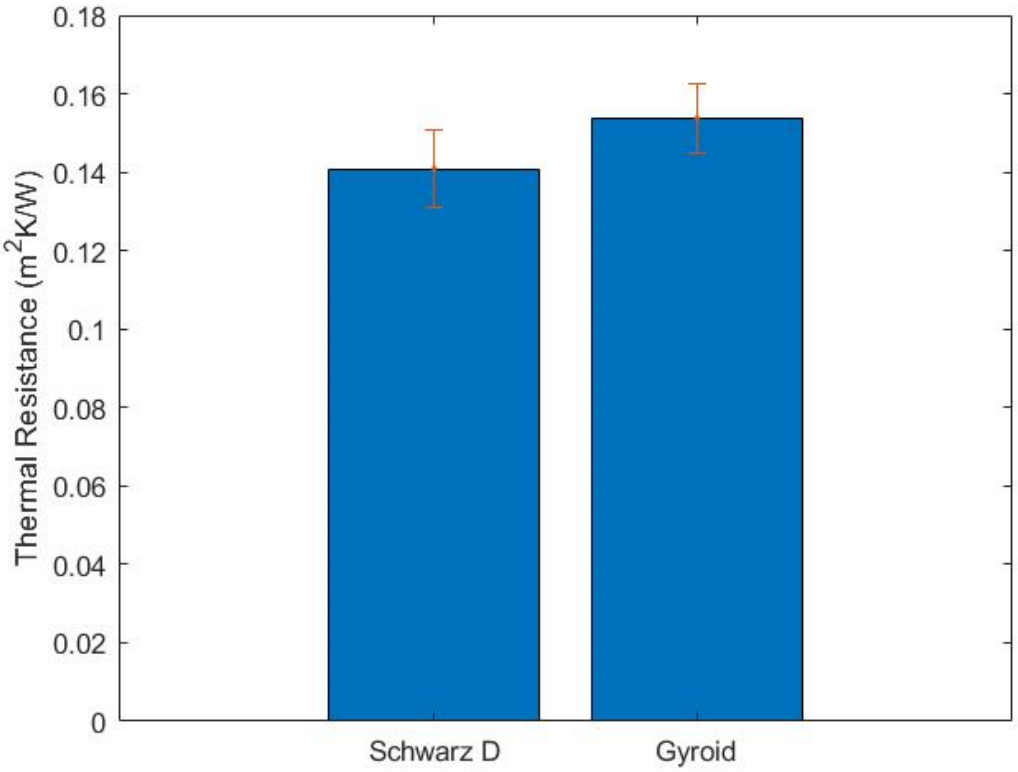

Figure 0.1. A Bar Plot Showing the Results of the First Experiment of the Thermal Resistances of Schwarz D and Gyroid without Electrolyte for Heat Flux of 769.795 Wm^{-2}

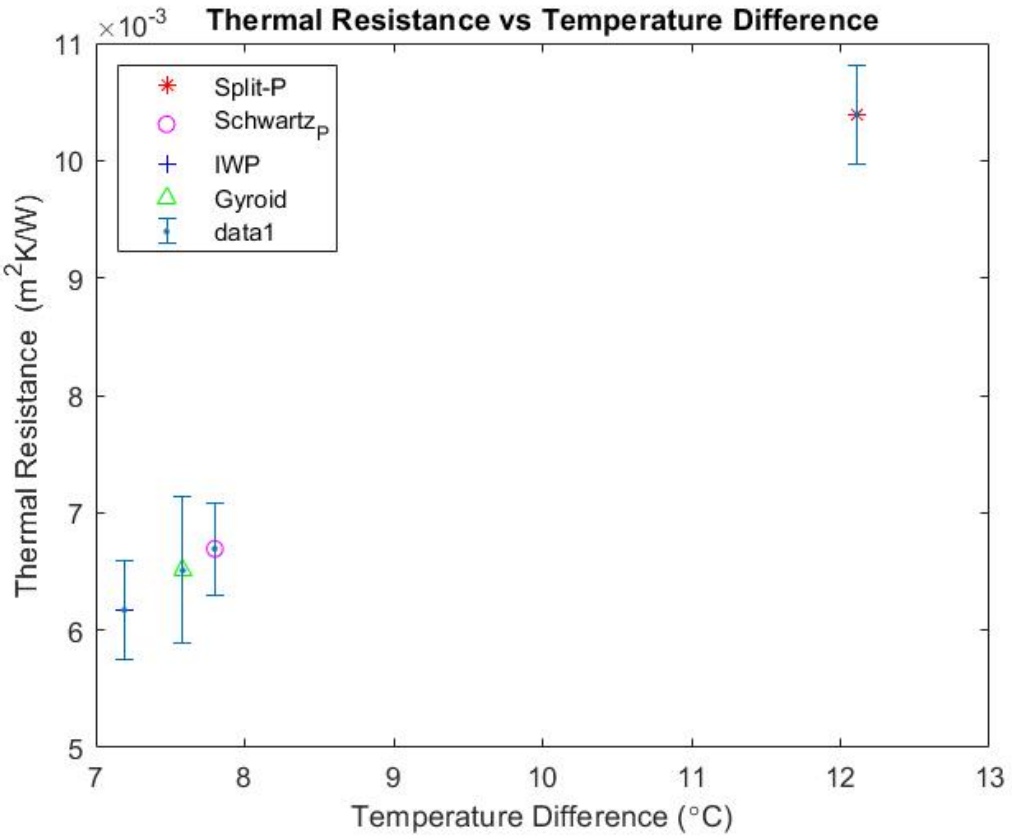

Figure 0.2. A Plot of Thermal Resistance Against Temperature Difference

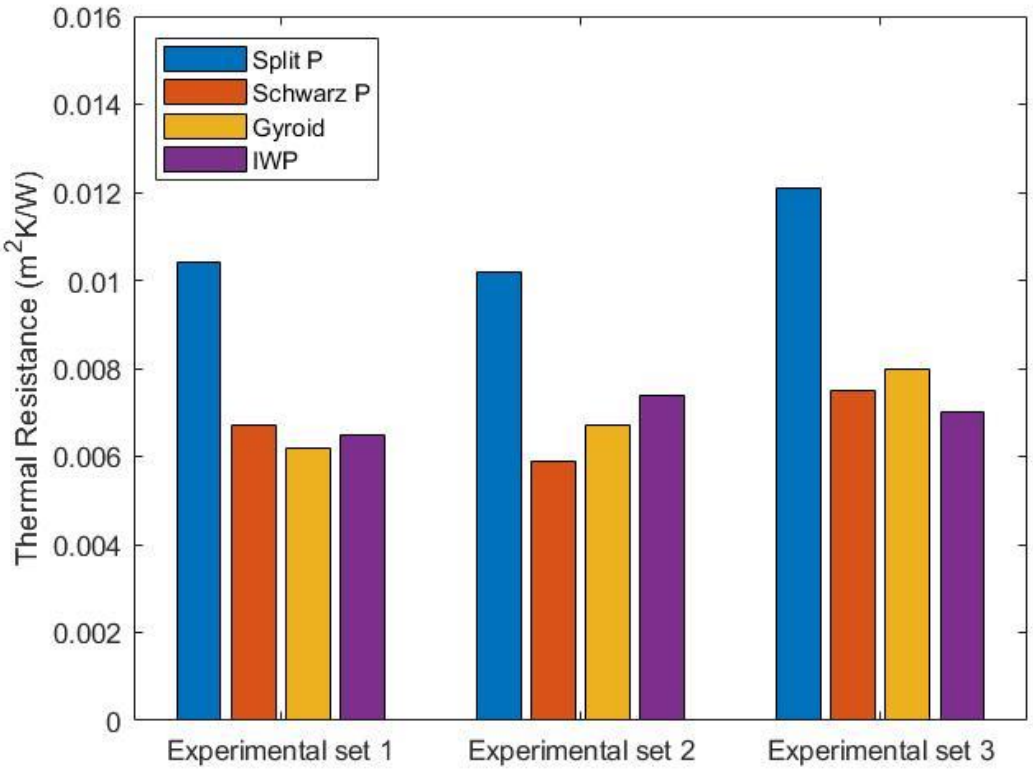

Figure 0.3. Plot of Thermal Resistance of The TPMS Structures for all the Three Sets of Experiment

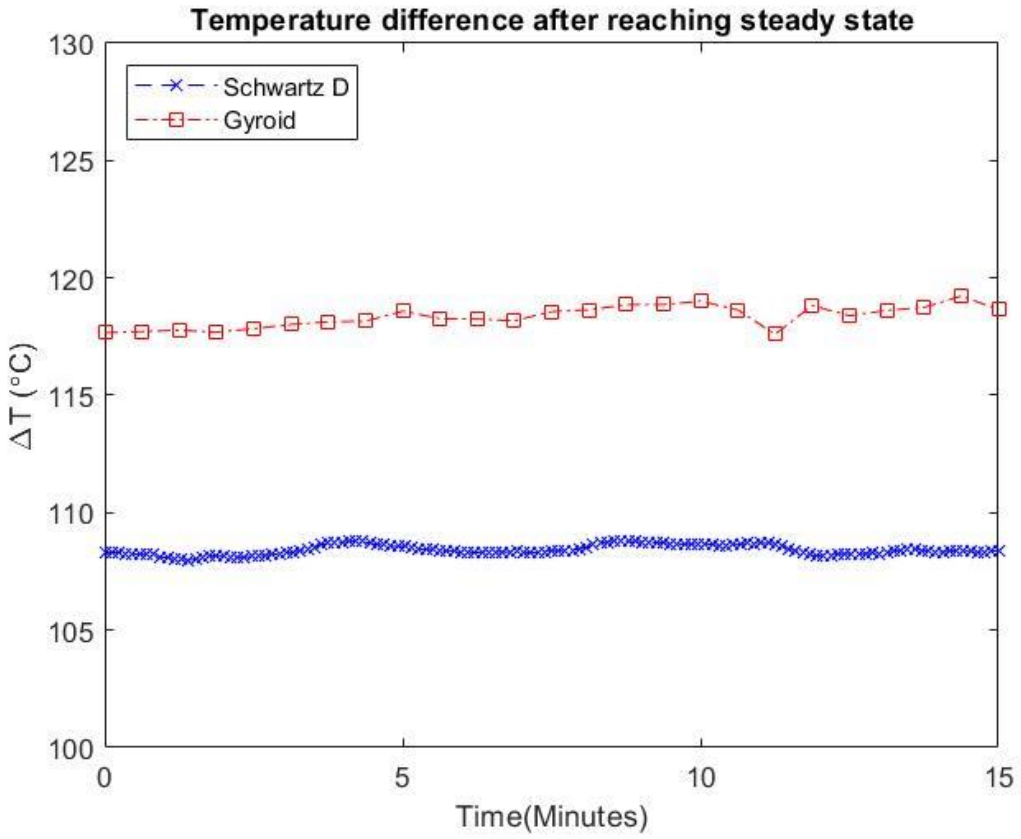

Figure 0.4. Plot of Temperature Difference for the Experiment without Electrolyte in the Thermogalvanic Cell After Steady State.